EES Batteries

PAPER

View Article Online
View Journal

Check for updates

Cite this: DOI: 10.1039/d6eb00059b

Synthesis, structure, stability, and ionic conductivity of $Na_5MSi_4O_{12}$ type solid electrolytes for solid-state sodium batteries

Anna Michalak,[a] Urvashi Urvashi,[a] Tom Dunlop,[b] Oliver Clemens[c] and M. Anji Reddy *[a]

Received 12th March 2026,
Accepted 10th May 2026

DOI: 10.1039/d6eb00059b

rsc.li/EESBatteries

$Na_5MSi_4O_{12}$-type silicates are emerging as functional solid electrolytes for solid-state sodium batteries due to their high ionic conductivity, combined with excellent chemical and electrochemical stability and low electronic conductivity. Understanding their synthesis, phase stability, crystal and electronic structures, and ionic conductivity and diffusion is essential for designing and developing better compounds. To this end, we investigated the synthesis, phase stability, structure, ionic and electronic conductivities, chemical and electrochemical stability, interfacial resistance, and Na metal deposition of four highly conducting solid electrolytes in the $Na_5MSi_4O_{12}$ series ($Na_5YSi_4O_{12}$, $Na_5DySi_4O_{12}$, $Na_5GdSi_4O_{12}$, and $Na_5SmSi_4O_{12}$). By analysing the results from synchrotron XRD, *in situ* high-temperature XRD, simultaneous thermal analysis, SEM, high-temperature electrochemical impedance spectroscopy, electronic structure calculations, chronoamperometry, and chronopotentiometry, we sought to establish correlations among these phases. This article will provide deep insight into the properties of NMS-type compounds.

Open Access Article. Published on 13 May 2026. Downloaded on 6/25/2026 9:59:45 AM.
This article is licensed under a Creative Commons Attribution-NonCommercial 3.0 Unported Licence.

Broader context

Sustainable and high-performing solid electrolytes are essential for developing safer solid-state batteries. $Na_5MSi_4O_{12}$-type solid electrolytes are very attractive due to their high ionic conductivity, combined with excellent chemical and electrochemical stability, and low electronic conductivity. They have high potential to replace the industrial-standard solid electrolyte, Sodium β-Alumina (BASE). However, their structure, phase stability, ionic conductivities, dendrite formation, electrochemical stability, and electronic structures are not well understood. Understanding these properties is vital to designing better solid electrolytes. In this article, we provide deep insight into the synthesis, phase stability, ionic conductivity, electronic structure, chemical and electrochemical stability, and dendrite formation, and diffusion of $Na_5MSi_4O_{12}$-type solid electrolytes by correlating results from Synchrotron XRD, *in situ* high-temperature XRD, thermal analysis, electrochemical impedance spectroscopy, theoretical calculations, linear sweep and cyclic voltammetry, and impedance evolution during metal deposition. This article will act as a modern reference in designing better solid electrolytes.

Introduction

Solid electrolytes (SEs) represent a major advancement over liquid electrolytes, as they improve battery safety, increase the Coulombic efficiency of metal deposition and stripping, reduce the solubility of electrode materials, and exhibit high ionic transport numbers.[1] This safety improvement is a reassuring step forward in energy storage.

In the context of sodium solid-state electrolytes, both polymer and inorganic systems have been widely explored, each presenting distinct advantages and limitations. Solid polymer electrolytes (SPEs) offer easy processing, excellent flexibility, and good interfacial contact with electrodes; however, their ionic conductivity at room temperature is typically limited ($\leq 10^{-5}$ S cm^{-1}), with acceptable conductivities (10^{-3}–10^{-4} S cm^{-1}) only achieved at elevated temperatures, where their mechanical stability is compromised.[2,3] Inorganic solid electrolytes, including sulphide-, halide-, and oxide-based materials, generally exhibit higher ionic conductivities compared to SPEs but face challenges related to stability and interfacial compatibility. Sulphide-based electrolytes, such as Na_3SbS_4 and Na_3PS_4 can achieve very high ionic conductivities (up to ~10^{-2} S cm^{-1})[4] and offer good processability due to their ductility, yet they suffer from poor air stability, narrow electrochemical windows, and instability against Na metal. Halide-based systems provide a wide electrochemical window, mechanical flexibility, and conductivities approaching 10^{-3} S cm^{-1}, but are similarly moisture-sensitive and unstable against Na electrodes.[2,3,5]

[a]IMPACT Energy Storage Laboratory, Faculty of Science and Engineering, Swansea University, Swansea, UK. E-mail: a.r.munnangi@swansea.ac.uk
[b]SPECIFIC, Faculty of Science and Engineering, Swansea University, Swansea, UK
[c]Materials Science, Materials Synthesis Group, University of Stuttgart, Stuttgart, Germany

© 2026 The Author(s). Published by the Royal Society of Chemistry

Open Access Article. Published on 13 May 2026. Downloaded on 6/25/2026 9:59:45 AM. This article is licensed under a Creative Commons Attribution-NonCommercial 3.0 Unported Licence.

Among oxide-based sodium solid electrolytes, Na-β-alumina (BASE) and NASICON ($Na_{1+x}Zr_2Si_xP_{3-x}O_{12}$) are widely regarded as the most promising candidates for solid-state sodium batteries.[6] Na-β-alumina exhibits exceptionally high ionic conductivity, reaching 0.4 S cm^{-1} at room temperature,[7] due to its layered structure that facilitates fast Na^+ transport; however, its practical application is constrained by its sensitivity to moisture, high processing temperatures, and interfacial resistance issues.[8–10] In contrast, NASICON-type electrolytes offer a three-dimensional Na^+ conduction framework, enabling relatively high ionic conductivities at room temperature (typically 10^{-4} S cm^{-1}), along with good chemical stability and a wide electrochemical stability window.[11,12] Nevertheless, like other oxide-based electrolytes, NASICON suffers from poor interfacial contact with electrodes and high interfacial resistance, as well as energy-intensive synthesis requirements to achieve a pure compound, which limit its overall performance and large-scale implementation.[13]

Compared to these established systems, $Na_5MSi_4O_{12}$-type (NMS) silicate compounds have emerged as particularly promising and are gaining importance due to their high ionic conductivity (ranging from 10^{-1} to 10^{-5} S cm^{-1} at 200 °C),[14] chemical and electrochemical stability, and low electronic conductivity, which are the most desirable properties for SEs in solid-state battery applications. A wide range of cations can be substituted in $Na_5MSi_4O_{12}$ (N5) at the M^{3+} site. The ionic conductivity of NMS-type compounds increases linearly with the ionic radii of M^{3+} cations,[14] reaching a maximum for Sm^{3+} (0.958 Å). Therefore, compounds containing larger cations, such as $Na_5YSi_4O_{12}$ (NYS), $Na_5DySi_4O_{12}$ (NDS), $Na_5GdSi_4O_{12}$ (NGS), and $Na_5SmSi_4O_{12}$ (NSS), are of particular interest due to their high ionic conductivity and anticipated electrochemical stability.

Despite these promising properties, several critical challenges remain in the synthesis and characterisation of NMS-type materials. One of the primary difficulties lies in obtaining phase-pure N5 compounds, as these materials are prone to forming structurally similar secondary phases such as $Na_3MSi_3O_9$ (N3) and $Na_9MSi_6O_{18}$ (N9) during synthesis.[14] These impurity phases are thermodynamically competitive within the Na_2O–M_2O_3–SiO_2 system and exhibit similar crystallographic features, making them difficult to distinguish.[15] The structural similarity and overlapping diffraction features of these phases complicate advanced characterisation and hinder the establishment of clear structure–property relationships. The presence of impurities significantly reduces the overall ionic conductivity due to their intrinsically poor Na^+ transport properties.[14,16] Furthermore, the N3 and N9 phases often act as intermediates prior to the formation of the desired N5 phase.[17–19] As a result, precise control over phase evolution and reproducible synthesis of phase-pure materials remain major challenges. Nevertheless, N5 phases have recently been successfully synthesised and investigated in solid-state sodium batteries.[4–10]

Among the NMS family, NYS is the most extensively studied composition.[20–24] Shannon *et al.* reported an ionic conductivity of 4×10^{-2} S cm^{-1} at 200 °C for NYS.[14] Recent studies demonstrated that ionic conductivity of 1.59×10^{-3} S cm^{-1} could be achieved at RT, with an activation energy of 0.20 eV, enabling improved cycling performance in NVP/NYS/Na cells.[21] Yang *et al.* used a tape-casting method to produce thin NYS sheets, achieving a conductivity of 1.0×10^{-3} S cm^{-1} with an activation energy of 0.30 eV. These thin sheets showed promising cyclic performance in Na/NYS/S batteries.[24] Despite its reported high ionic conductivity of 6×10^{-2} S cm^{-1} at 200 °C.[14] Studies on NDS remain limited. In this report, we synthesised and investigated NDS, alongside other NMS phases. Recently, we demonstrated the synthesis of pure NGS with an ionic conductivity of 1.99×10^{-3} S cm^{-1} at RT.[25] As expected from the cation-size trend, NSS exhibits the highest ionic conductivity in this series. Recent reports have shown ionic conductivities as high as 2.9×10^{-3} S cm^{-1} at RT, with an activation energy of 0.15 eV.[26] Further improvements were achieved by incorporating an amorphous matrix between NSS grains, resulting in a conductivity of 5.61×10^{-3} S cm^{-1}.[27] However, the electrochemical stability of NSS against Na metal remains a concern.[14] In this work, we investigated the synthesis process, phase stability, structure, ionic and electronic conductivities, chemical and electrochemical stabilities, electronic structure, Na^+ diffusion, interfacial resistance, and Na metal deposition behaviour of NYS, NDS, NGS, and NSS under similar processing conditions, with the aim of establishing clear correlations among these phases.

Synthesis and phase stability of $Na_5MSi_4O_{12}$-type compounds

To understand the synthesis process and phase stability of NMS, we conducted simultaneous thermal analysis (STA) on ball-milled precursor mixtures used to synthesise NMS phases, as well as on the synthesised NMS phases. While STA results do not fully replicate the conditions in a typical muffle furnace due to differences in processing conditions and heat transfer, they provide a good general indication of mass losses, heat release associated with phase formation, phase changes, and melting behaviour. Fig. 1 presents the thermal analysis results of ball-milled precursors used to synthesise NMS phases and of synthesised NMS phases in the temperature range of 100–1300 °C.

$$5/2Na_2CO_3 + {}^1/_2M_2O_3\,(M = Y,\ Gd,\ Sm\ and\ DY) + 4SiO_2 \rightarrow Na_5MSi_4O_{12} + 5CO_2 \quad (1)$$

Interestingly, all four compounds showed similar thermal behaviours. Eqn (1) illustrates the reaction of the precursor mixture used in synthesising NMS phases. These precursor mixtures include Na_2CO_3, M_2O_3 (where M = Y, Dy, Gd, and Sm), and SiO_2. During heating, decomposition of starting powders occurs, leading to a predictable mass loss due to CO_2 release, as shown in eqn (1). The only expected gas release during this process is CO_2 from the thermal decomposition of Na_2CO_3. Based on the molecular weight of $Na_5MSi_4O_{12}$, a mass loss of 16 to 17% is anticipated due to CO_2 emission. However, a 19–20% mass loss was observed, with the extra 3–4% attributed to the removal of absorbed species, such as residual moist-

© 2026 The Author(s). Published by the Royal Society of Chemistry

Open Access Article. Published on 13 May 2026. Downloaded on 6/25/2026 9:59:45 AM.
This article is licensed under a Creative Commons Attribution-NonCommercial 3.0 Unported Licence.

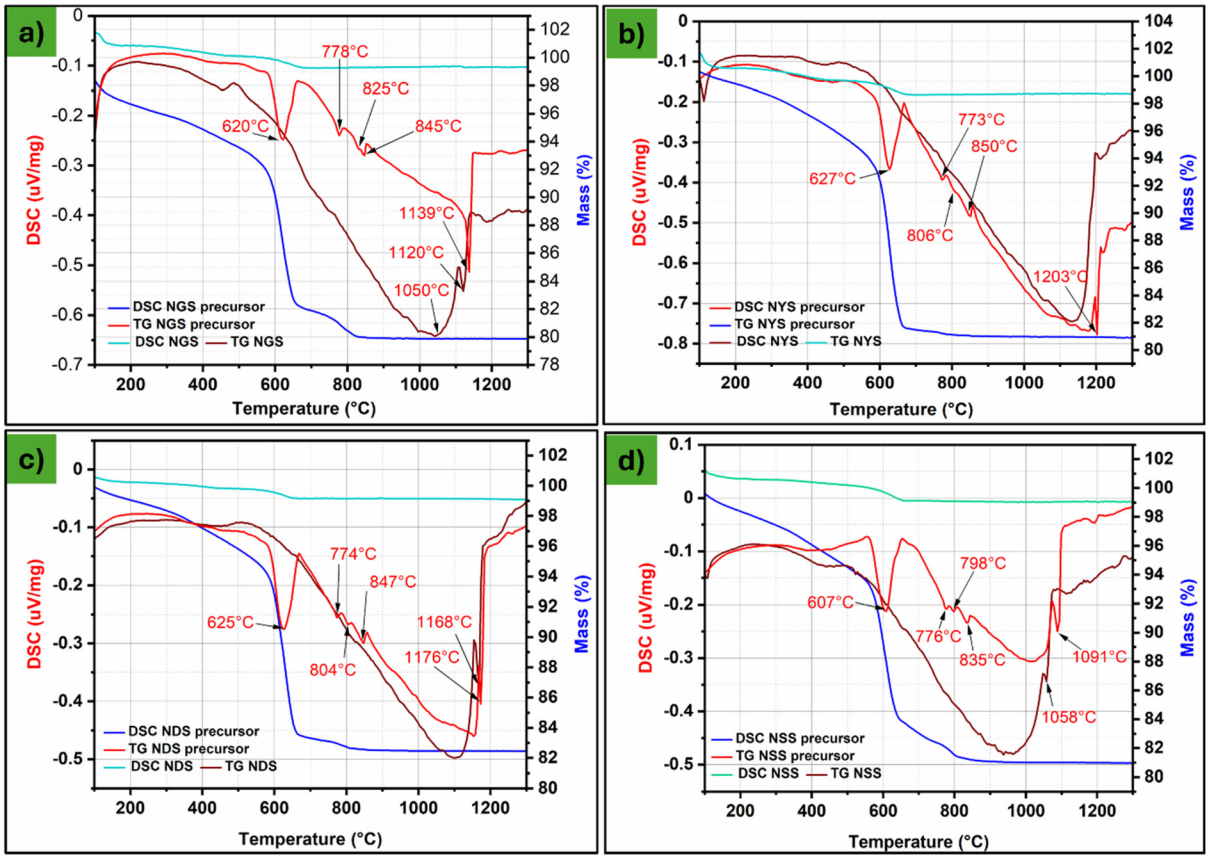

Fig. 1 Thermogravimetry (TG) and differential scanning calorimetry (DSC) curves of (a) NGS precursor and synthesised NGS; (b) NYS precursor and synthesised NYS; (c) NDS precursor and synthesised NDS; (d) NSS precursor and synthesised NSS.

ure. Endothermic peaks associated with CO_2 release were detected between 600 and 630 °C. All four compounds exhibited three additional endothermic peaks beyond the CO_2-loss peak. The endothermic peak at 778 °C for NGS (773 °C for NYS, 774 °C for NDS, and 776 °C for NSS) corresponds to the weight loss observed between 750 °C and 800 °C.

The small endothermic peak observed at 825 °C for NGS (806 °C for NYS, 804 °C for NDS, and 798 °C for NSS) is attributed to the formation of the N9 phase. The endothermic peak at 845 °C for NGS (850 °C for NYS, 847 °C for NDS, and 835 °C for NSS) is linked to the transformation of N9 into the N5 phase. The sharp endotherms correspond to the melting of NMS phases (1139 °C for NGS, 1225 °C for NYS, 1176 °C for NDS, and 1091 °C for NSS). A maximum mass loss of 1% was observed for synthesised NMS at around 600 °C, likely due to the loss of adsorbed water. This shows that these compounds are highly stable after synthesis. For synthesised NMS, a broad endotherm peak followed by a sharp endothermic peak was observed. The broad endothermic peak indicates particle growth of NMS, while the sharp endotherm relates to the melting of NMS (1120 °C for NGS, 1203 °C for NYS, 1168 °C for NDS, and 1058 °C for NSS).

To understand the phase formation temperatures of the N3, N5, and N9 phases, ball-milled NGS precursor powders were heated to various temperatures (700 °C, 800 °C, 900 °C, 1000 °C, 1050 °C, and 1100 °C), held for 4 hours, and then allowed to cool to RT. Fig. 2a shows the X-ray diffraction (XRD) patterns of these samples. At 700 °C and 800 °C, the N9 phase is dominant. Upon heating above 800 °C, the N9 phase begins transforming into the N5 phase. These observations are consistent with the STA results. At 1000 °C, the N5 phase becomes predominant, with minor impurities observed from the N9 phase. The fraction of the N9 phase reaches a minimum at 1000 °C, but then increases again at 1050 °C and 1100 °C. Since NGS melts at approximately 1120 °C, XRD measurements could not be taken beyond 1100 °C. The N5 phase of NGS remains highly stable between 850 °C and 1050 °C, and a synthesis temperature of 1000 °C is recommended. Additionally, quenching NGS from 1050 °C was found to stabilise phase-pure NGS, with no detectable N9 impurities. We also performed *in situ* high-temperature XRD on ball-milled NGS precursor powders to understand the dynamics of phase formation. Fig. 2d displays the HT-XRD patterns of the NGS precursor material, recorded over a temperature range from 700 °C to 1100 °C, with the final pattern recorded after cooling to RT. It is assumed that at 700 °C, the primary phase present is N9-, with the observed peaks corresponding to this phase. This phase remains dominant at 800 °C and 900 °C, and as

Open Access Article. Published on 13 May 2026. Downloaded on 6/25/2026 9:59:45 AM.
This article is licensed under a Creative Commons Attribution-NonCommercial 3.0 Unported Licence.

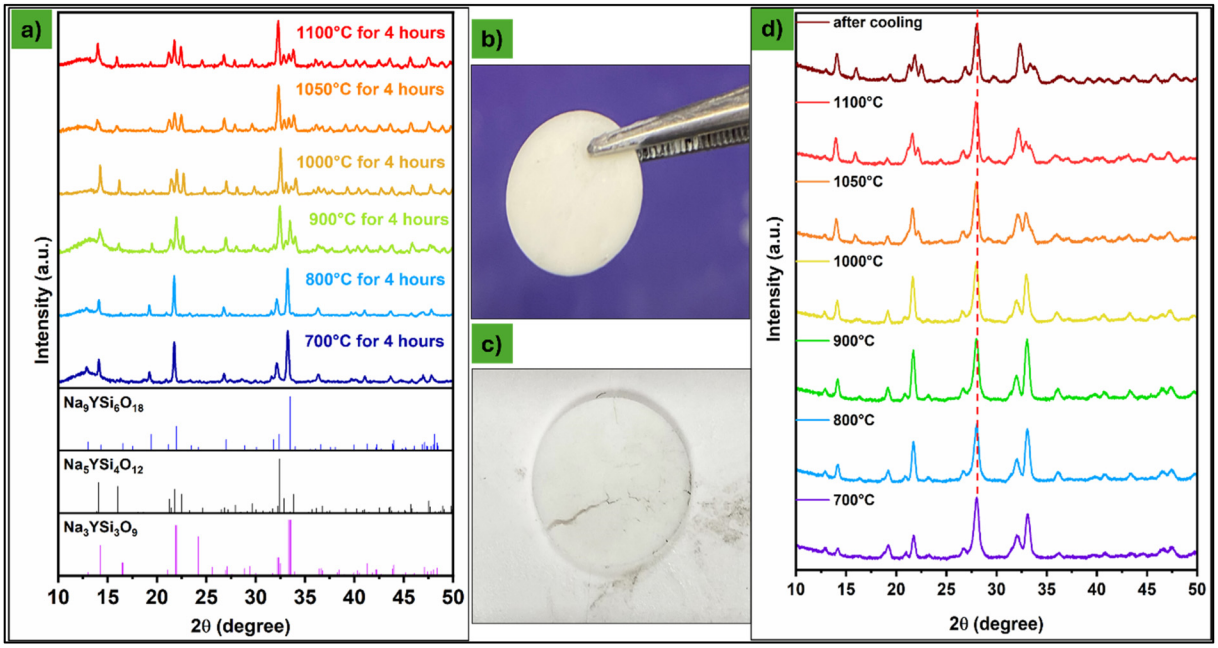

Fig. 2 (a) XRD patterns of ball-milled NGS precursor powders heated at various temperatures (700 °C, 800 °C, 900 °C, 1000 °C, 1050 °C, and 1100 °C), held for 4 hours. (b) NGS solid electrolyte pellet and (c) the pellet after sintering at 1100 °C and (d) *in situ* HT XRD patterns of NGS precursor (the dashed red line is due to the graphite dome used, which is unchanged). The XRD pattern of the graphite dome is shown separately in Fig. S1.

the sintering temperature increases, peaks belonging to new compositions begin to appear. While the patterns remain largely unchanged up to 1000 °C, at 1050 °C peaks associated with the N5 phase begin to appear. This transformation appears to be largely complete by 1100 °C. After cooling to room temperature, small peaks attributed to the N9-phase are observed at 19.5° and 33.5°, while the remaining peaks are associated with the N5-phase.

It is also important to determine the thermal stability of the synthesised SEs to incorporate them into the full battery production process. The STA results for synthesised N5 samples indicate that they are thermally stable (Fig. 1). To further verify this, we performed high-temperature XRD on pre-synthesised NGS and NYS samples. Fig. 3a displays the XRD patterns of synthesised NGS at various temperatures, measured *in situ* in a heating chamber. The peaks at 33.5 degrees (indicated with a red arrow) correspond to the N9 phase. The N5 phase remains highly stable below 900 °C, but the N9 phase reappears at 900 °C. This aligns with observations made during NGS synthesis. The HT XRD patterns of the synthesised NYS are shown in Fig. 3b. Synthesised NYS is quite stable until below 1100 °C. However, a peak corresponding to the N9 phase was observed after cooling.

SEM micrographs of sintered NGS pellets (Fig. S2) reveal a well-sintered, dense surface with a consistent texture, indicating material homogeneity. Some surface roughness and minor porosity are observed. Higher-magnification images show a granular structure with irregularly shaped grains tightly packed, though some voids are present between them. The SEM micrographs of NYS display a uniform surface with irregularly distributed pores. At higher magnification, a granular structure is evident, with small, closely packed grains separated by varying-sized voids. In contrast, NDS exhibits a smoother, denser surface with fewer visible pores. Higher magnification images of NDS reveal a tightly packed granular structure similar to NYS, with pores distributed throughout the material. The NSS surface appears coarser, with larger particles of varying shapes and sizes packed together. At higher magnification, the NSS surface exhibits a crystalline structure, with well-defined, sharp-edged grains of various sizes and more prominent grain boundaries. The particles in the NSS sample are significantly larger compared to those in the NGS, NYS, and NDS samples.

The density of crystallised NGS was approximately 3.09 g cm^{-3}, corresponding to about 96% of its theoretical density (3.21 g cm^{-3}). Similarly, the density of crystallised NYS was approximately 2.70 g cm^{-3}, corresponding to ~94% of its theoretical density (2.86 g cm^{-3}). The density of NDS was calculated to be 3.11 g cm^{-3}, corresponding to ~96% of its theoretical density (3.25 g cm^{-3}). The density of NSS was measured as 2.89 g cm^{-3}, corresponding to ~91% of its theoretical density (3.16 g cm^{-3}). Please note that these densities are estimated through Archimedes' principle.

Structure of NMS-type compounds

In this context, it is worth having a clearer look at the structure of these silicates. Silicates with a Si : O ratio of 1 : 3 can have different connectivity of the tetrahedrally coordinated silicon ions *via* corners. This can lead to the formation of infinite chains described by a connectivity scheme of $(SiO_{2/2}O_{2/1})_\infty$

© 2026 The Author(s). Published by the Royal Society of Chemistry

Open Access Article. Published on 13 May 2026. Downloaded on 6/25/2026 9:59:45 AM. This article is licensed under a Creative Commons Attribution-NonCommercial 3.0 Unported Licence.

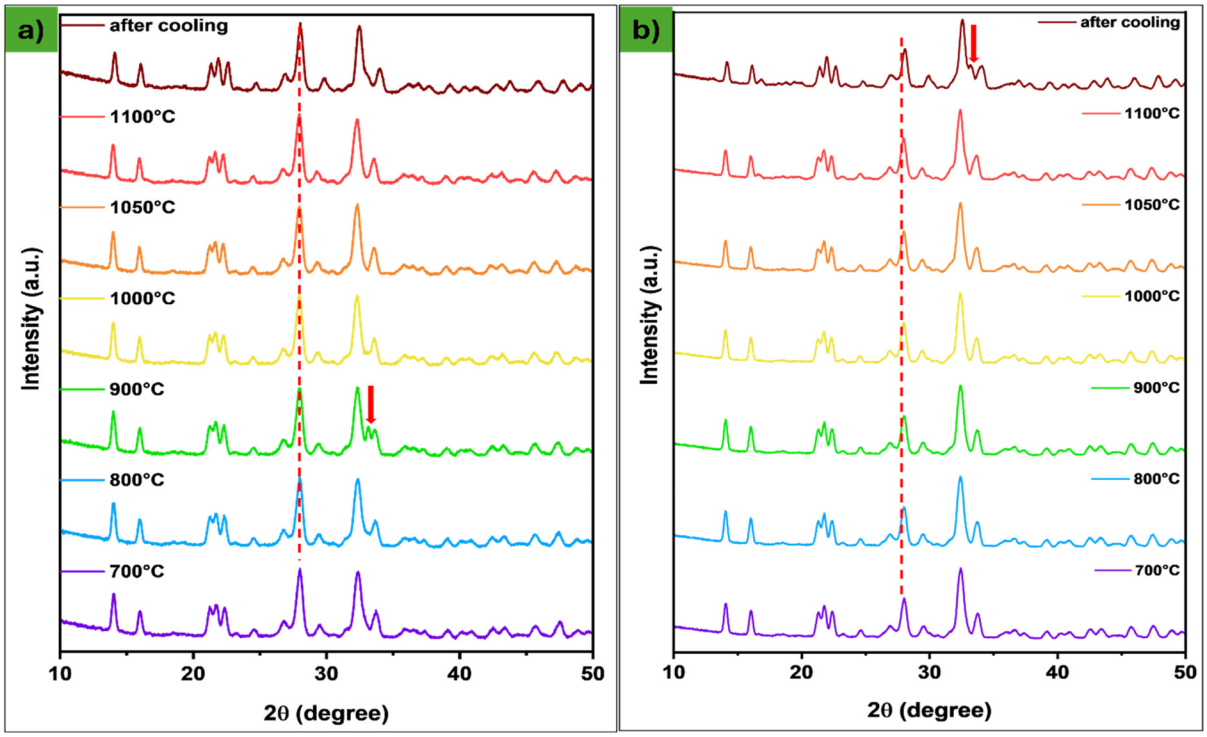

Fig. 3 XRD patterns of synthesised NGS and NYS heated at various temperatures (the dashed red line is due to the graphite dome used, which is unchanged); (a) NGS and (b) NYS. Please note that the XRD pattern of the synthesised sample (after cooling) slightly shifted to higher angles. The misalignment can be referred to as the sample changing height due to thermal expansion/contraction. The XRD pattern of the graphite dome is shown separately in Fig. S1.

according to Niggli's scheme. Alternatively, rings can also be formed *via* a similar connectivity scheme, leading to building units $(SiO_{2/2}O_{2/1})_n$ with $n \in$ IN* and $n \leq 3$. Whereas the N5 phase with space group $R\bar{3}c$ can be classified as a ring silicate with rings composed of 6 corner-sharing silicate units, the N3/N9 phases reported are chain silicates with infinite chains. Though the structural motifs of N5 and N9/N3 are different, the composition of these compounds can be basically described with a chemical formula $Na_{(2-3x)*n}M_{x*n}(SiO_3)_n$ with $0 \leq x \leq 2/3$ and $n \in$ IN*. Thus, all these compositions could be described as a binary cut through the ternary phase equilibrium diagram of the components M_2O_3–Na_2O–SiO_2 (Fig. 4).

If one compares the cubic structure (s.g. $Pa\bar{3}$) found for $Na_9M(SiO_3)_6$ to the orthorhombic structure (s.g. $P2_12_12_1$) of $Na_3M(SiO_3)_3$, both being chain silicates, a simple analysis *via* group – subgroup relationships shows that these structures are related *via* two *translationengleiche* transitions ($Pa\bar{3} \rightarrow P2_13 \rightarrow P2_12_12_1$) and possess the same connectivity scheme of the silicate subnetwork. However, N9/N3 distinguishes with respect to the overall Na + M cation content, and the positioning of the M cations in relation to the $(SiO_{2/2}SiO_{2/1})_\infty$ chains. If one compares the structural datasets of the N9 phase reported for $Na_{8.12}Y_{1.293}(SiO_3)_6$[28] and of the N3 phase reported for $Na_3Y(SiO_3)_3$.[29] One can derive possible limits of the composition of these samples. If all crystallographic Na + Y cation sites would be fully occupied, one ends up with a composition of $Na_9M(SiO_3)_6 = Na_{3/2}M_{1/6}(SiO_3)$, *i.e.* (Na + M)/Si = 10/6 = 1.667; in contrast, if the crystallographic sites which are occupied by M in the N9 or N3 phase (*i.e.* 8 atoms per unit cell $Pa\bar{3}$ equivalent to ~1/8 1/8 1/8, 8 atoms per unit cell $Pa\bar{3}$ equivalent to 3/8 3/8 3/8 and 4 atoms per unit cell $Pa\bar{3}$ equivalent to 0 0 0 (these sites are indicated as orange polyhedra in the lower part of Fig. 5)) would be occupied by M, this could even lead to overall lower (Na + M)/Si content compositions than $Na_3M(SiO)_3 = Na_1M_{1/3}(SiO_3)$ ((Na + M)/Si = 4/3 = 1.333) such as $Na_{4/5}M_{5/12}(SiO_3)$ ((Na + M)/Si = 78/60 = 1.3). This compositional flexibility is visualized in Fig. 4. Similar considerations can be done for the trigonal ring silicate $Na_5M(SiO_3)_4$ (s.g. $R\bar{3}c$), and lead to a maximum cation content equivalent to the N9 compound $Na_9M(SiO_3)_6 = Na_{3/2}M_{1/6}(SiO_3)$, *i.e.* (Na + M)/Si = 10/6 = 1.667, under the condition that the 18e site of M can be partly occupied by Na either and that other Na sites are fully occupied. Similarly, a cation-poor composition can be imagined if the 18*e* site is fully occupied by M, leading to $Na_5M(SiO_3)_4$; for the N9 compound, no previous reports indicate that any site other than 18e was occupied by M cations. Again, this compositional flexibility is visualized in Fig. 4.

Further insight into the detailed structure and composition of the N5 phases is obtained by high-resolution synchrotron XRD. The refined synchrotron XRD patterns of $Na_5M(SiO_3)_4$ (M = Y, Dy, Gd, Sm) compounds are shown in Fig. 6. In contrast to the diffraction patterns recorded on laboratory diffractometers,

© 2026 The Author(s). Published by the Royal Society of Chemistry

Open Access Article. Published on 13 May 2026. Downloaded on 6/25/2026 9:59:45 AM.
This article is licensed under a Creative Commons Attribution-NonCommercial 3.0 Unported Licence.

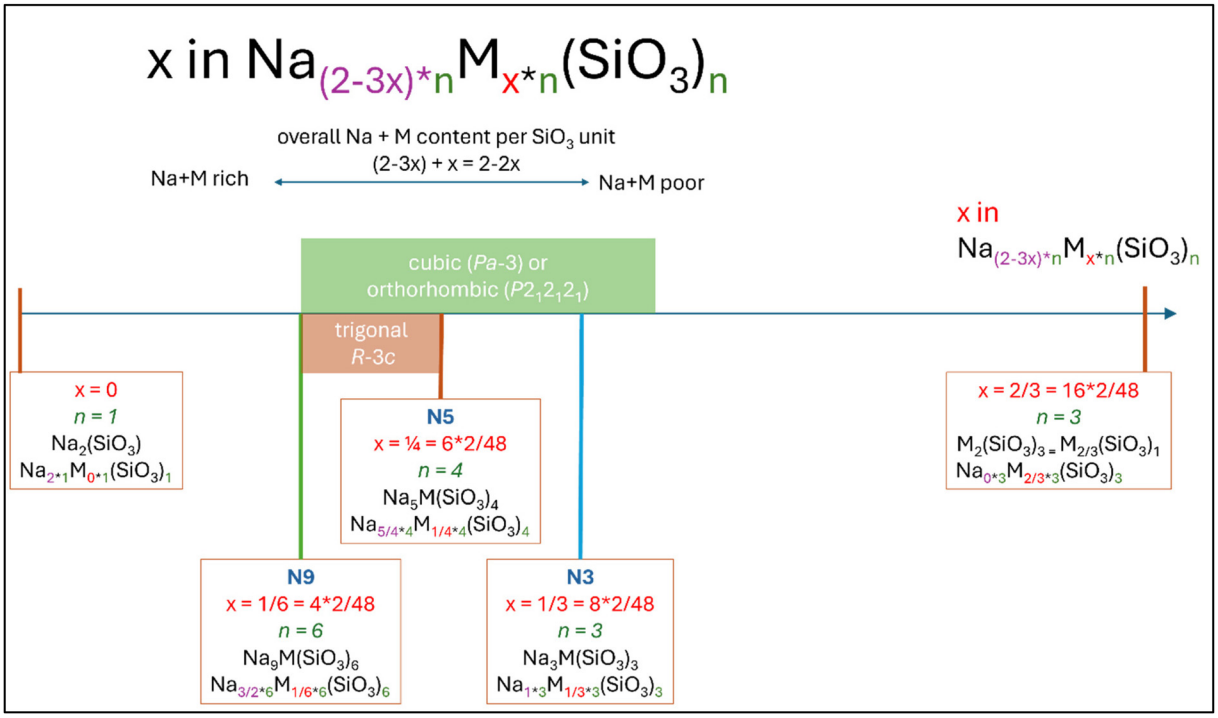

Fig. 4 Compositional flexibility of different chain and ring silicates.

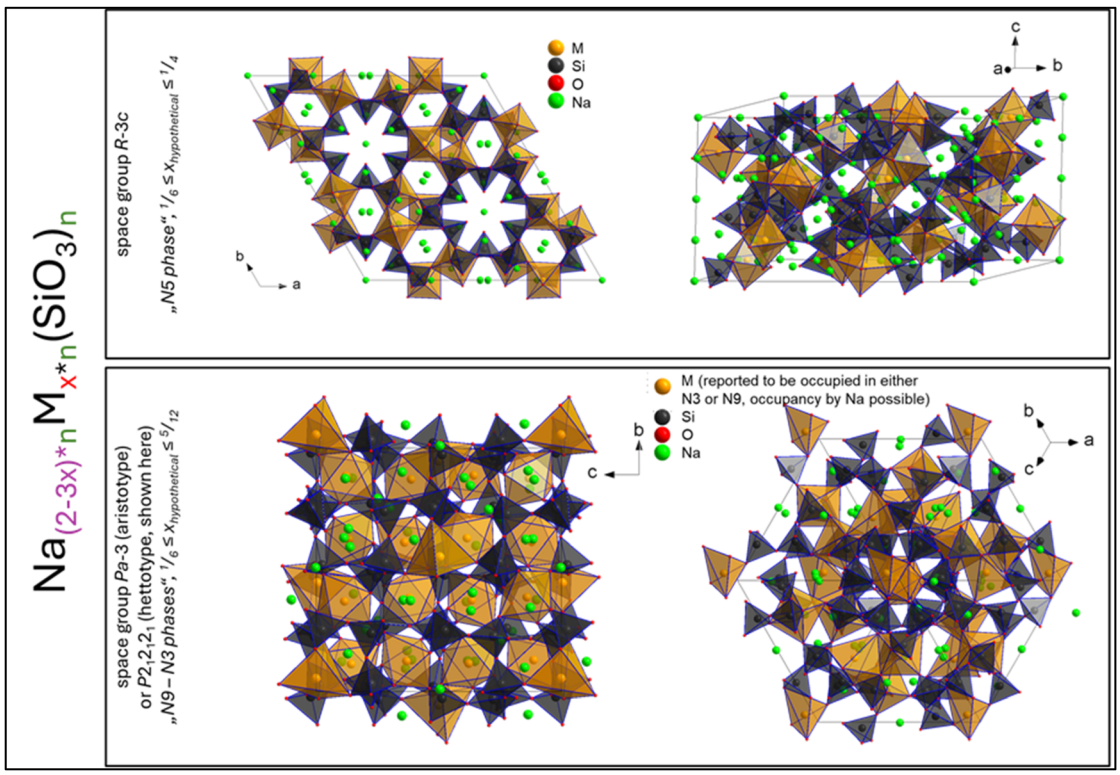

Fig. 5 Crystal structure of the trigonal N5 phase (top) as well as the cubic/orthorhombic N9/N3 phases (bottom) shown on the example of the orthorhombic phase. Sites which are reported to be occupied by M cations in ref. 30 are given as orange polyhedra.

© 2026 The Author(s). Published by the Royal Society of Chemistry

Open Access Article. Published on 13 May 2026. Downloaded on 6/25/2026 9:59:45 AM.
This article is licensed under a Creative Commons Attribution-NonCommercial 3.0 Unported Licence.

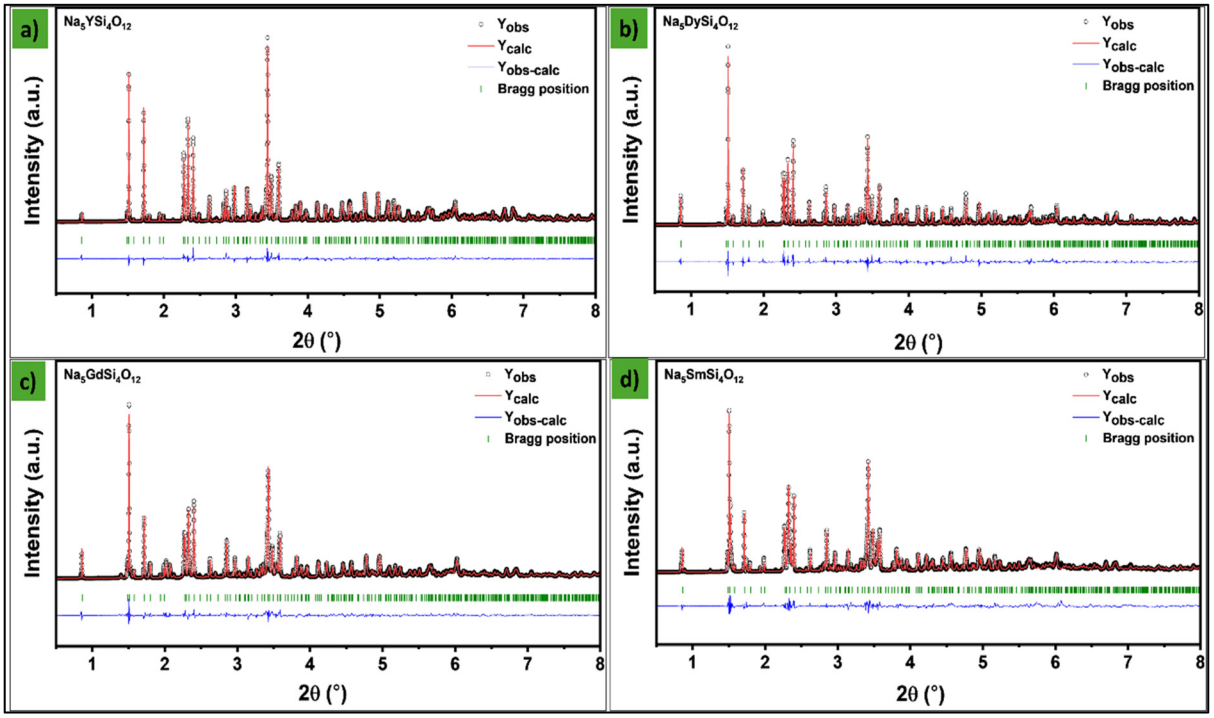

Fig. 6 Plots of SXRD data fitted with structural models for the trigonal $R\bar{3}c$ type phase of $Na_{5+d}M_{1-d/3}(SiO_3)_4$ (resp. $Na_{(2-3x)*n}M_{x*n}(SiO_3)_n$) for (a) $Na_5YSi_4O_{12}$, (b) $Na_5DySi_4O_{12}$, (c) $Na_5GdSi_4O_{12}$ and (d) $Na_5SmSi_4O_{12}$. Bragg markers are given for the trigonal phase; reflections corresponding to unidentified phases and/or N5 phase are not marked explicitly here and were fitted by pseudo-Voigt functions to estimate the overall area corresponding to impurity phases as given in Table 1.

the high intensity counts and signal-to-noise ratios enable a more detailed analysis and the detection of impurity phases beyond the N9 phase. These impurities could not be assigned, even after indexing attempts. However, we estimated the overall impurity amount by integrating the intensities of impurity-phase reflections (unknown plus N9) relative to the main N5 phase. The main parameters of the refined data are given in Table 1. In addition, Rietveld analysis of synchrotron XRD (Fig. 6) data revealed that the 18e site occupancy by M^{3+} ions decreased with increasing ionic radius. Thus, this indicates that M-rich compositions of the N5 structure are favoured for smaller cations such as Y and Dy, whereas larger cations, such as Gd and especially Sm, lead to significant amounts of impurity phases. The structural analysis to reveal the highest-quality structural information is hindered, especially for M = Gd and Sm, because the impurity phases could not be well assigned and overlap with the reflections of the N5 phase. However, the presence of other phases led to the assumption that the N5 phase composition might deviate, as discussed in the previous section. Thus, we allowed for a small compositional deviation according to $Na_{5+3x}M_{1-x}(SiO_3)_4$, with additional sodium sites partly occupying the M site and the partly occupied Na sites. Though the improvement of R_{wp} is small (usually in the order of up to 0.1%) and thus must be taken with caution, x appears to deviate from 0 only when there are impurity phases present, in principle agreement with the phase width considerations described in the previous section.

We further analysed the structure of N5 phases to provide more insight into the origin of its high ionic conductivity. All

Table 1 Synchrotron XRD refinement results of NMS

NMS	Lattice parameters [Å]	Cell volume [Å^3]	Refined composition	Intensity of reflections corresponding to phases other than the N5 phase (cubic N9 + unknown impurities) [%]
NYS	a = 22.0172(4) c = 12.6334(3)	5303.6(2)	$Na_5YSi_4O_{12}$	0.3
NDS	a = 22.0647(4) c = 12.6269(3)	5323.8(2)	$Na_{5.09}Dy_{0.97}Si_4O_{12}$	2.0 (to a small part corresponding to an N9 phase with phase fraction of ~1 wt% relative to N5 phase)
NGS	a = 22.1091(4) c = 12.6695(3)	5363.2(2)	$Na_{5.21}Gd_{0.93}Si_4O_{12}$	6.4 (mainly corresponding to an N9 phase with phase fraction of ~11 wt% relative to N5 phase)
NSS	a = 22.1494(4) c = 12.6926(3)	5392.6(2)	$Na_{5.06}Sm_{0.98}Si_4O_{12}$	16.4 (to a smaller part corresponding to an N9 phase with phase fraction of ~6 wt% relative to N5 phase)

Open Access Article. Published on 13 May 2026. Downloaded on 6/25/2026 9:59:45 AM.
This article is licensed under a Creative Commons Attribution-NonCommercial 3.0 Unported Licence.

compositions crystallise in the same trigonal structure, with the rare-earth cation occupying a single crystallographic site. The M cations (Gd1, Y1, Sm1, or Dy1) occupy the 18*e* Wyckoff position (~0.25, 0, $\frac{1}{4}$). Two crystallographically distinct silicon sites, Si1 and Si2, are located at 36*f* Wyckoff positions, while all oxygen atoms (O1–O6) occupy 36*f* sites, forming the rigid ring silicate framework. Sodium ions are distributed over multiple crystallographic sites with more or less distorted octahedral coordination with varying occupancies; the sodium ions on 6*a* (32 site symmetry) and 6*b* (−3 site symmetry) are well localised and fully occupied. Similarly, the 36*f* site (1 site symmetry) shows high occupancy close to 1, whereas the 18*e* site (2 site symmetry) (~0.72, 0, $\frac{1}{4}$) and the 36f site (~0.33, ~0.14, ~0.09) show much stronger deviations from full occupancy and larger displacement parameters. The latter most likely indicates that these sites, due to their partial occupancy, also contribute mainly to the high sample conductivities. We speculate that the Na ions in the 18e site are likely to occupy the metal site, as it is closer to the metal site. We acknowledge that a slightly different position of sodium ions, an increased number of sites, *etc*., can also be used to describe the electron density distribution derived from the bad localisation of these Na^+ cations; thus, the reader must be aware that a well-ordered Na^+ substructure does not represent the material sufficiently well at ambient temperature.

Ionic and electronic conductivity of NMS-type compounds

The Na^+ ionic conductivities of NGS, NYS, NDS, and NSS were evaluated using EIS. Solid electrolyte pellets were sputtered with gold on both sides to serve as blocking electrodes, and their impedance was measured over the 30–120 °C temperature range. The impedance spectra for NGS, NYS, NDS, and NSS over the full temperature range are shown in Fig. 7. The small semicircle in the EIS spectrum is attributed to the total resistance of the NMS solid electrolyte, including both bulk and grain boundary resistance. At the same time, the spike represents charge build-up at the Au electrode. The total resistance, *R*, was determined from the fitted data as the intercept of the semicircle with the *x*-axis and was found to be 64 Ω for NGS, 68 Ω for NYS, and 59 Ω for NDS. In contrast, NSS has a total resistance of around 193 Ω at 30 °C. The ionic conductivities of all compounds were then calculated, and the full results for the 30–120 °C temperature range are presented in Table S3. NSS exhibits the lowest conductivity among the four studied compounds, with a value of 6.13×10^{-4} S cm^{-1} at 30 °C. NYS has an ionic conductivity of 1.56×10^{-3} S cm^{-1}, while NGS and NDS exhibit comparable conductivities of 1.99×10^{-3} S cm^{-1} at 30 °C. This trend persists across the studied 30–120 °C temperature range, with NGS slightly outperforming NDS at elevated temperatures.

Based on these results, a correlation between the ionic conductivity of the M element in $Na_5MSi_4O_{12}$ and the ionic conductivity of the final compound can be established. The ionic conductivity of $Na_5MSi_4O_{12}$ (where M = Y, Dy, Gd, Sm) increases progressively with the ionic radius of M^{3+}, as depicted by the ionic radii of the rare-earth elements: Y^{3+} = 0.9 Å < Dy^{3+} = 0.912 Å < Gd^{3+} = 0.938 Å < Sm^{3+} = 0.958 Å. In the NMS crystal structure, the $Si_{12}O_{36}$ rings are held apart by the

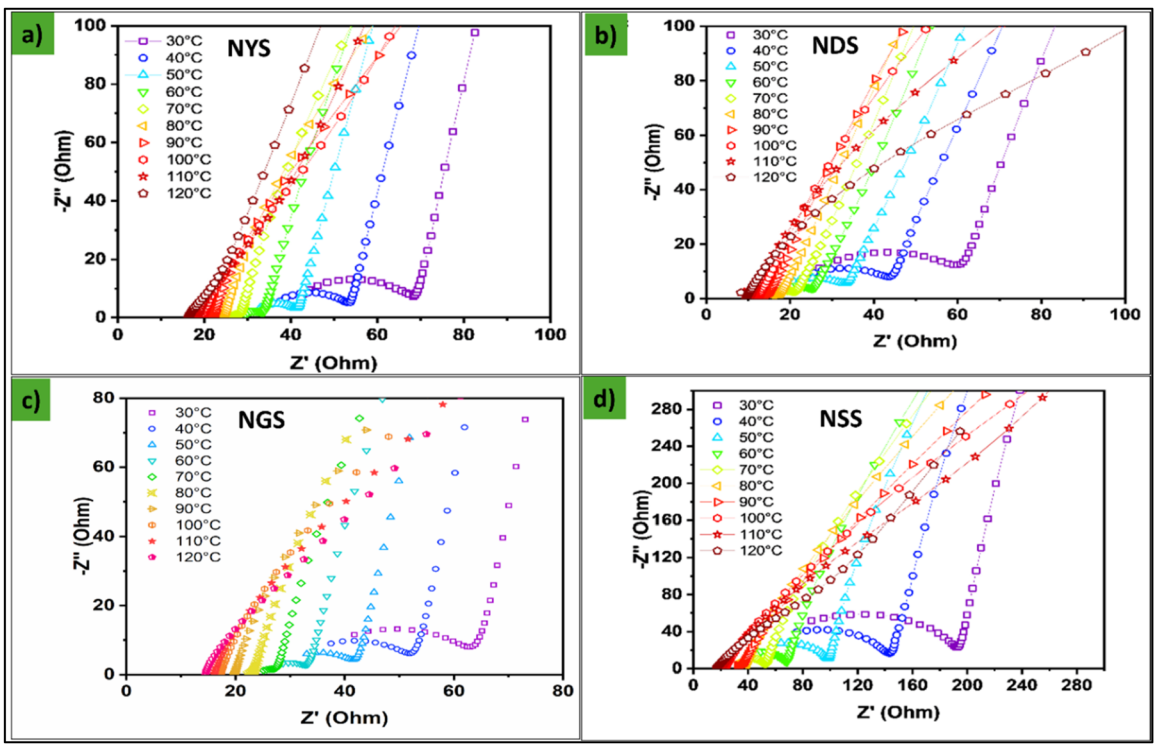

Fig. 7 The Nyquist plot for the NMS series in the temperature range of 30–120 °C; (a) NYS, (b) NDS, (c) NGS, and (d) NSS.

© 2026 The Author(s). Published by the Royal Society of Chemistry

Open Access Article. Published on 13 May 2026. Downloaded on 6/25/2026 9:59:45 AM. This article is licensed under a Creative Commons Attribution-NonCommercial 3.0 Unported Licence.

MO_6 octahedra, so the size of the M^{3+} ion largely determines the amount of "open" space between rings. A direct relationship exists between cell volume and ionic radius: a larger M^{3+} ionic radius increases the 3D channel area for Na^+ ions, facilitating their movement and increasing their concentration.

However, despite this general trend, the Sm^{3+}-containing compound, with the largest ionic radius of 0.958 Å, exhibits the lowest ionic conductivity in the series. This finding is inconsistent with recently reported results, where the NSS compound was found to display the highest ionic conductivity among sodium silicate solid electrolytes.[27] However, similar behaviour was reported in earlier studies by Beyeler *et al.*, where Sm-containing compound exhibited lower ionic conductivities than both NGS and NYS.[31] These observations suggest that, for the synthesis process used in this study, the size of Sm^{3+} may be a limiting factor in forming the desired N5 Phase of the $Na_5MSi_4O_{12}$ compounds. The critical channel size may be reached with Sm^{3+} ions, reducing ionic conductivity. Additionally, a higher amount of the amorphous phase may be present in the Sm^{3+} compound, contributing to the lower conductivity, as suggested by the XRD analysis.

The temperature-dependent ionic conductivities were plotted in Arrhenius diagrams and linearly fitted (Fig. 8a, c, e and g) to determine activation energies E_a. The total E_a of NGS calculated is 0.17 eV, 0.16 eV for NYS, 0.22 eV for NDS, and 0.26 eV for NSS. The increase in E_a for NSS can be attributed to the lower ionic conductivity measured in this study compared to the typically higher values reported in the literature.

The electronic conductivities, σ_{el}, of NGS, NYS, NDS, and NSS were determined by DC polarisation experiment, with the results shown in Fig. 8b, d, f and h.

$$\sigma_{el} = \frac{d \times I}{A \times U}$$

where σ_{el} is the electronic conductivity (in S cm^{-1}), d is the thickness of the solid electrolyte pellet (in cm), I is the final stabilised current (in A), A is the area of the solid electrolyte pellet (in cm^2), and U is the applied voltage (in V).

A very low electronic conductivity of 2.70×10^{-10} S cm^{-1} was obtained for NGS, approximately seven orders of magnitude lower than its ionic conductivity, indicating negligible electronic conduction. Similarly, NSS exhibits an ultralow electronic conductivity of 7.43×10^{-12} S cm^{-1}, while NYS and NDS show values of 6.78×10^{-10} S cm^{-1} and 2.22×10^{-9} S cm^{-1}, respectively. All compounds demonstrate negligible electronic conductivity relative to their ionic conductivities.

Chemical and electrochemical stability of NMS-type compounds

As shown in Fig. 1, a maximum mass loss of 1% was observed for pre-synthesised NMS at around 600 °C, likely due to the loss of adsorbed water. This shows that these compounds are highly stable after synthesis. XRD patterns of NMS exposed to air and water for different lengths of time are shown in Fig. S3. None of the NMS decomposed upon exposure to air or stirring in water. XRD patterns broadened due to surface amorphization due to the absorption of water. But the amorphous nature disappeared after heat treatment at 1000 °C, confirming that these compounds can be stored in ambient conditions for a longer period.

The electrochemical stability of NYS, NDS, NGS, and NSS was evaluated using both linear sweep voltammetry (LSV) and cyclic voltammetry (CV). The results are shown in Fig. 9. The LSV was measured from open-circuit voltages (about 2.0 V *vs.* Na^+/Na for NYS, NDS, and NGS, and about 0.0 V *vs.* Na+/Na for NSS) to 8.0 V *vs.* Na^+/Na. All solid electrolytes maintain a stable electrochemical window with no significant signs of oxidation within these ranges. The electrochemical stability was further characterised by using CV. CV ran in the voltage window of −0.5 to 6.0 V *vs.* Na^+/Na. No oxidation or reduction peaks were observed, except for the Na metal deposition and stripping between −0.5 and 0.5 V. This wide electrochemical window enables the use of a broader selection of higher-voltage cathode materials, which benefits the overall energy density of the full battery. These experiments demonstrate that these compounds are exceptionally chemically and electrochemically stable.

Sodium plating, stripping, and insight into dendrite formation in NMS-type electrolytes

The ability to reversibly deposit and strip sodium metal uniformly at lower potentials and higher current densities is an essential characteristic of sodium solid electrolytes for battery applications. To conduct these measurements, NMS SEs were evaluated in a symmetrical Na/NMS/Na cell. Fig. 10 illustrates the Na deposition and stripping behaviour of NYS, NDS, NGS, and NSS through the evolution of cell voltage profiles as a function of current measured at 25 °C. The current was reversed at 30 minute intervals, with deposition and stripping conducted for 8 hours at each step. The current density was increased stepwise from 0.1 to 0.5 mA cm^{-2} after every 8 hour cycle. During the Na plating and stripping process, Na^+ ions shuttle through the solid electrolyte and are deposited or extracted from the metallic anode. It is expected that Na metal will deposit along the grain boundaries of the solid electrolytes, particularly at higher current rates. As the current rate increases, this deposition and stripping become less efficient, leading to potential dendrite growth and increasing the risk of short circuits in the cell.

The Na/NYS/Na symmetric cell exhibited an initial resistance of about 170 Ω. The initial voltage response was almost 0.022 V at a current density of 0.1 mA cm^{-2}. The cycling profile of the Na/NYS/Na cell exhibited ohmic current–voltage behaviour at the initial current for the first 3 hours, with some polarisation observed thereafter, although the voltage remained low at 0.023 V. This small polarisation may indicate the onset of sodium dendrite growth within the cell. The polarisation was approximately equal for both polarities, and the impedance decreased to 160 Ω after 8 hours of cycling at 0.1 mA cm^{-2}. Upon increasing the current density to 0.2 mA cm^{-2}, more pronounced polarisation was observed, and the resistance further decreased to about 130 Ω by the end of this cycling stage. This

Open Access Article. Published on 13 May 2026. Downloaded on 6/25/2026 9:59:45 AM.
This article is licensed under a Creative Commons Attribution-NonCommercial 3.0 Unported Licence.

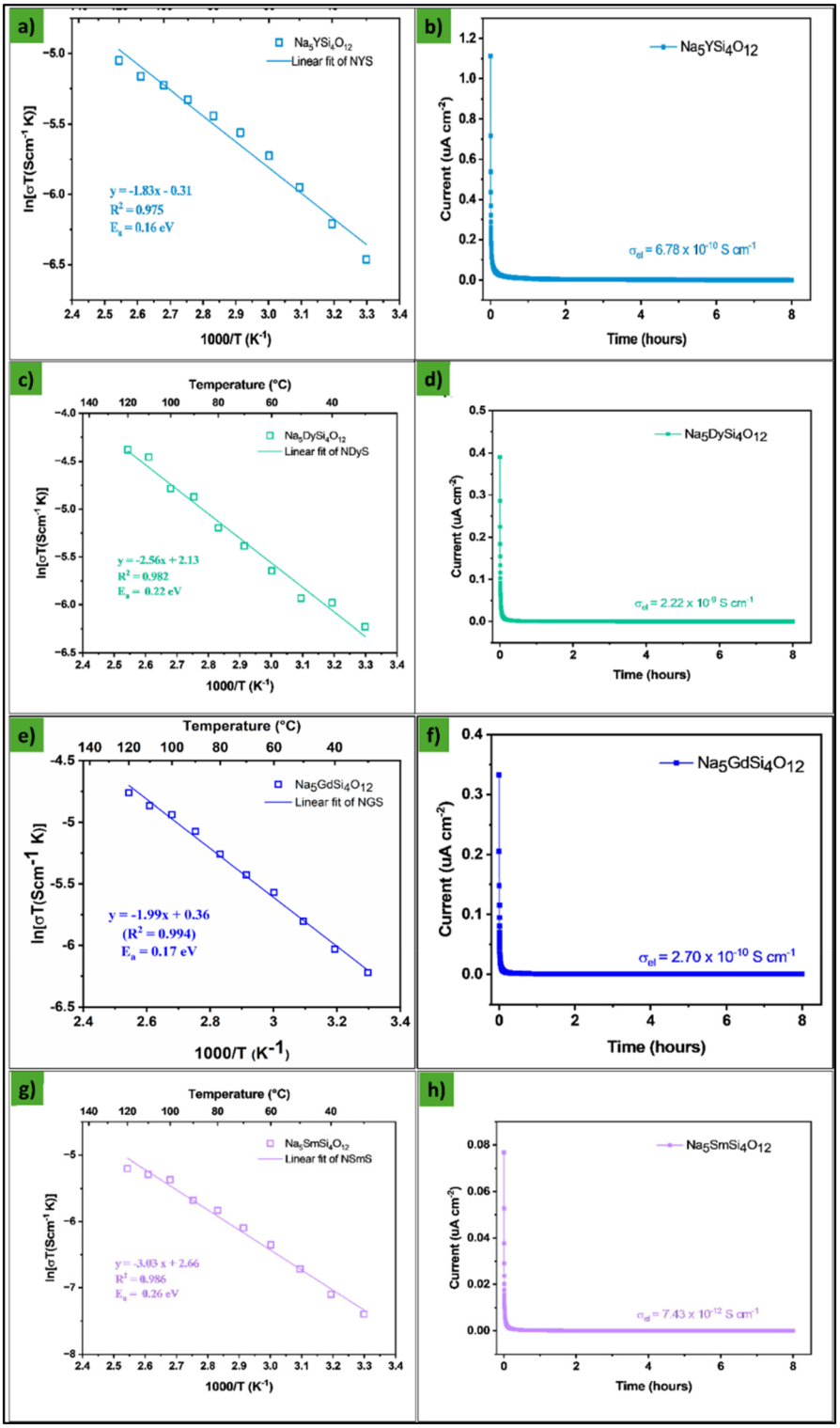

Fig. 8 Arrhenius plot for the ionic conductivity of NMS series and the time *vs.* current plot for the determination of electronic conductivity of the NMS series; (a) and (b) NYS; (c) and (d) NDS; (e) and (f) NGS; (g) and (h) NSS.

trend continued as the current was raised to 0.3 mA cm^{-2}, at which a more dramatic, yet still symmetric, polarisation was observed, and the impedance remained at 130 Ω. However, when the current density was increased to 0.4 mA cm^{-2}, the polarisation effects became even more pronounced and were no longer equal on both sides, as the voltage began to oscillate slightly. At this stage, the impedance increased to 160 Ω. Further voltage fluctuations were observed at a current density

© 2026 The Author(s). Published by the Royal Society of Chemistry

Open Access Article. Published on 13 May 2026. Downloaded on 6/25/2026 9:59:45 AM.
This article is licensed under a Creative Commons Attribution-NonCommercial 3.0 Unported Licence.

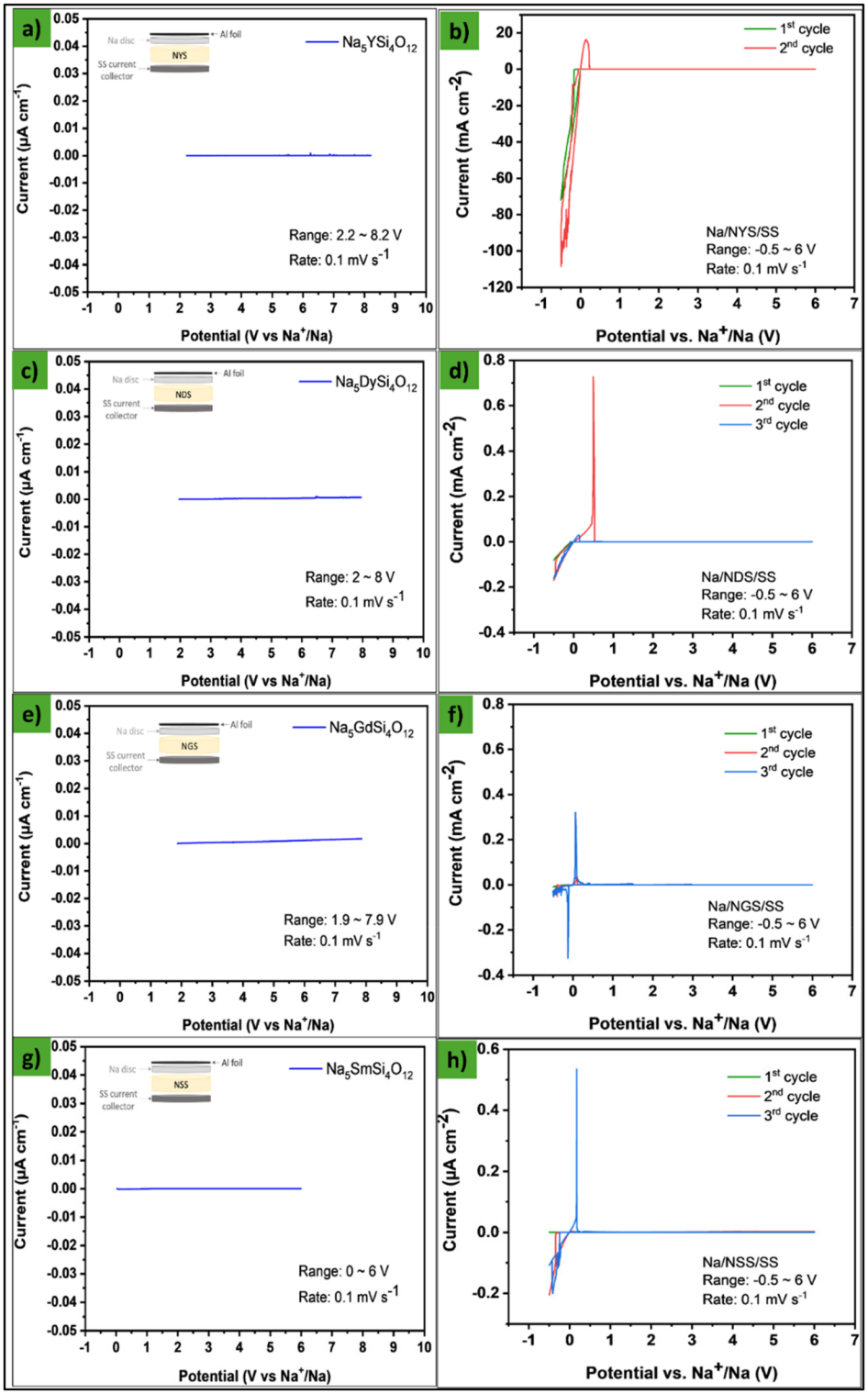

Fig. 9 LSV and CV of NMS series; (a) and (b) NYS; (c) and (d) NDS; (e) and (f) NGS; (g) and (h) NSS.

of 0.5 mA cm^{-2}. After cycling the cell at this current density for 4 hours, a sudden drop in cell voltage from 0.310 V was observed, and the impedance decreased to 20 Ω. Despite these irregular behaviours, the potential did not drop to 0 V, and cycling was observed at about 0.013 V. The impedance did not reach 0 Ω, indicating that the cell was not completely short-circuited. A digital mustimeter confirmed the absence of a short circuit.

© 2026 The Author(s). Published by the Royal Society of Chemistry

Open Access Article. Published on 13 May 2026. Downloaded on 6/25/2026 9:59:45 AM.
This article is licensed under a Creative Commons Attribution-NonCommercial 3.0 Unported Licence.

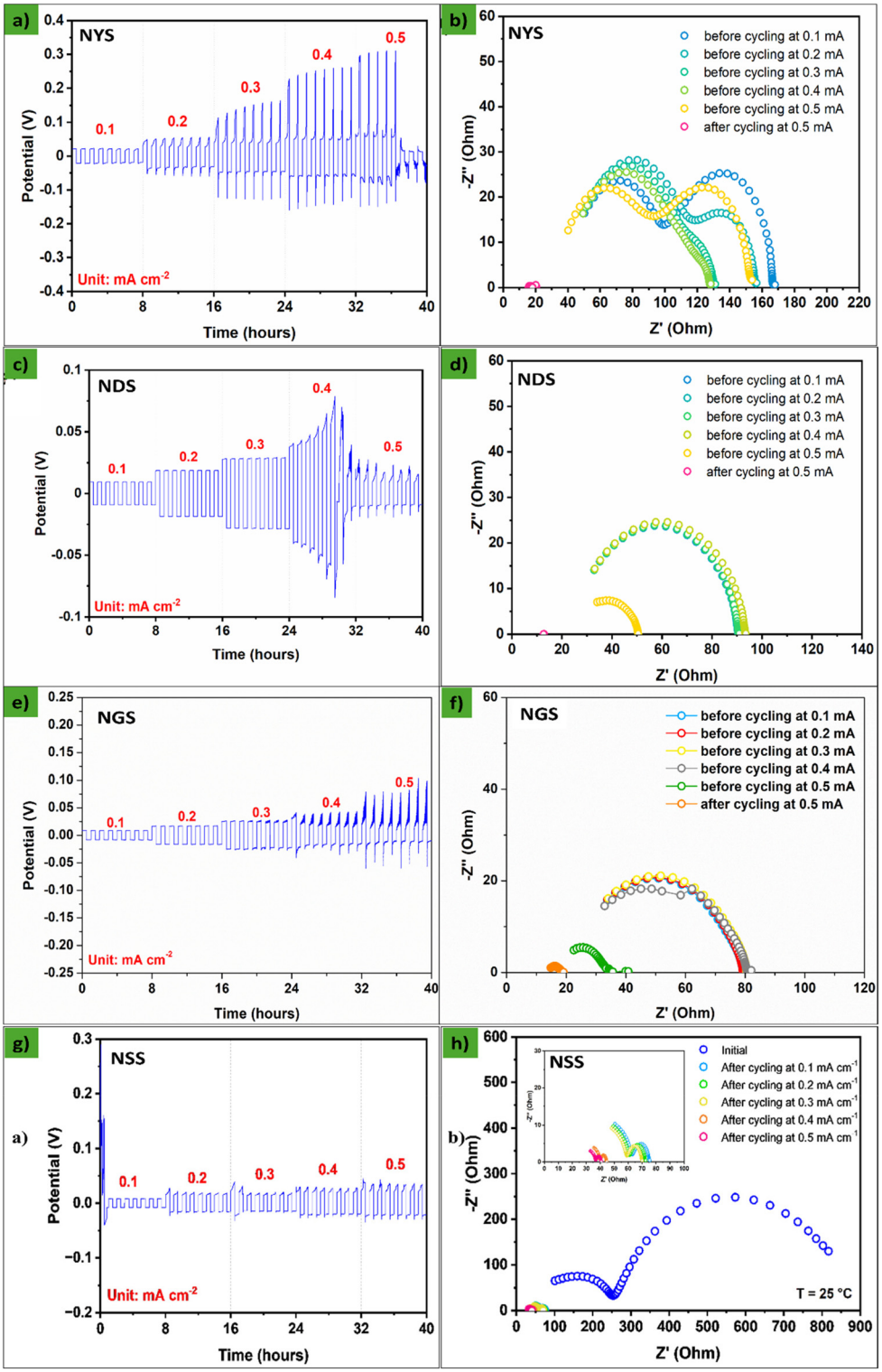

Fig. 10 Chronopotentiometry and EIS studies of (a) and (b) Na/NYS/Na; (c) and (d) Na/NDS/Na; (e) and (f) Na/NGS/Na; (g) and (h) Na/NSS/Na cells.

Before cycling, the Na/NDS/Na cell exhibited a resistance of about 90 Ω, and the initial voltage response was 9 mV at the current density of 0.1 mA cm^{-2}. The cycling profile of this symmetric cell also followed ohmic current–voltage behaviour, with no increase in voltage or other significant changes observed over the 0.1 to 0.3 mA cm^{-2} current density range during 24 hours of testing. There was also no change in the cell's resistance, indicating that NDS is stable against sodium

© 2026 The Author(s). Published by the Royal Society of Chemistry

Open Access Article. Published on 13 May 2026. Downloaded on 6/25/2026 9:59:45 AM.
This article is licensed under a Creative Commons Attribution-NonCommercial 3.0 Unported Licence.

metal under these conditions. However, after increasing the current density to 0.4 mA cm^{-2}, polarisation increased, and the cell resistance decreased to about 50 Ω after 8 hours of cycling at this current density. Similar to NYS, even after further increasing the current density to 0.5 mA cm^{-2}, the potential did not drop to 0 V, and the impedance did not reach 0 Ω, avoiding total short-circuiting of the cell. The gradual increase in voltage and the nonlinear behaviour at higher current densities imply inhomogeneous dissolution and deposition of metallic Na during cycling.

The Na/NGS/Na symmetric cell exhibited smooth, stable sodium deposition and stripping behaviour over a current density range of 0.1–0.3 mA cm^{-2}, with an initial overpotential of 8 mV at 0.1 mA cm^{-2}. The deposition overpotential increased proportionally with increasing current density. At 0.4 mA cm^{-2}, voltage fluctuations appeared, and the interfacial resistance decreased to 40 Ω after 8 h. Further increases in current density led to increased voltage noise and a further reduction in resistance to 20 Ω. Although the resistance decreased at higher current densities, none of the cells short-circuited over the investigated current range. The reduction in resistance is likely associated with sodium metal penetration or dendrite formation within the solid electrolyte.

The EIS spectrum of the Na/NSS/Na symmetric cell consists of one partially resolved small semi-circle in the higher frequency region and a larger semi-circle in the low frequency region. Extrapolating the large semicircle to the *x*-axis shows that the cell exhibited an unusually high initial resistance of about 900 Ω. The initial stripping from the uncycled Na foil caused an abrupt voltage increase to approximately 0.25 V, which was significantly higher than in the other cells studied. The highest voltage, and thus the highest resistivity, was measured only at the beginning of the first cycle. After this initial behaviour, the cell displayed a stable cycling profile, with interfacial resistance decreasing to 75 Ω after 8 hours of cycling at 0.1 mA cm^{-2} (inset of Fig. 10h). The voltage remained stable, and the interfacial resistance showed minor changes during the subsequent two cycling stages at 0.2 and 0.3 mA cm^{-2}. After raising the current density to 0.4 mA cm^{-2}, a more pronounced overpotential was observed, and after 8 hours of cycling, the resistance decreased to 45 Ω. Similar behaviour is observed during cycling at 0.5 mA cm^{-2}, and by the end of the measurement, the resistance has decreased to 40 Ω. This voltage behaviour suggests sodium dendrite growth within the electrolyte, but as with the other cells, the Na/NSS/Na symmetric cell did not short-circuit during the experiment.

The EIS measurements indicate that NMS-type materials can achieve low interface resistances with metallic sodium. However, the Na/NSS/Na cells exhibited an unusually high initial interfacial resistance that decreased upon cycling. The primary contributor to the impedance in Na symmetric cells is the charge transfer at the electrode–electrolyte interface. A possible explanation for this high initial resistance is the low effective interfacial area, likely due to incomplete contact between the sodium metal and the electrolyte. The observed reduction in impedance during cycling is a common phenomenon and can be attributed to improved electrode wetting, where the plated sodium improves the contact at the solid electrolyte–Na side. Nonetheless, further detailed studies are needed to fully understand why this behaviour was specific to NSS cells.

Among the assembled symmetric cells, Na/NGS/Na and Na/NSS/Na cells exhibit a rather stable voltage profile, whereas Na/NYS/Na and Na/NDS/Na cells show more irregularities. The observed decrease in polarisation voltage of Na/NYS/Na and Na/NDS/Na symmetric cells during cycling at higher currents could be attributed to a phenomenon known as "soft short-circuit" or "soft breakdown", which has been observed in metal batteries, particularly at higher currents.[32–35] The possible dendrite formation and growth mechanism in NMS-type solid electrolytes is depicted in Fig. 11a. Soft shorts in solid-state batteries are subtle and not fully understood. Soft short-circuit involves a partial short circuit in which a low-resistance bridge is formed, and both ionic and electronic conduction

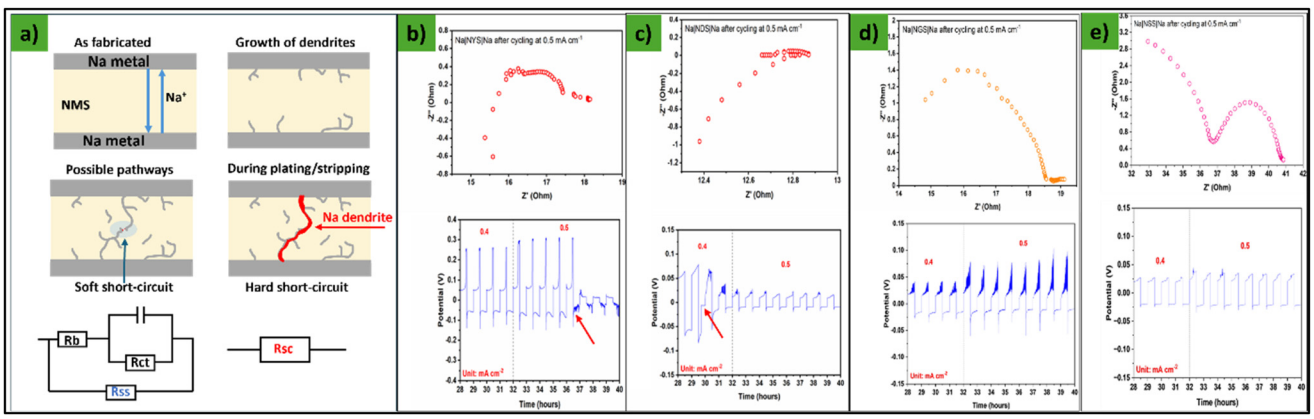

Fig. 11 (a) Schematic of possible Na dendrite growth, penetration, and short-circuiting mechanism, and proposed equivalent circuits for soft and hard short-circuit (drawn based on ref. 32–34); the EIS spectrum of NMS post-Na plating/stripping test and the voltage profiles during the last 12 hours of cycling; (b) NYS, (c) NDS, (d) NGS and (e) NSS.

© 2026 The Author(s). Published by the Royal Society of Chemistry

Open Access Article. Published on 13 May 2026. Downloaded on 6/25/2026 9:59:45 AM. This article is licensed under a Creative Commons Attribution-NonCommercial 3.0 Unported Licence.

are present in the cell (Fig. 11a). This contrasts with a complete short circuit, or "hard breakdown", in which a continuous path with very low resistance forms, causing all the current to flow through it and leading to cell failure. Ideally, in solid-state cells, only ions should act as charge carriers. However, during a soft short-circuit, unintended electronic conduction occurs due to the formation of conductive pathways, such as dendrites, that enable electron transport alongside ion transport. These filaments are very small metal dendrites that penetrate the solid electrolyte and maintain high electronic resistance due to their small size, preventing a dramatic drop in overpotential during cycling and avoiding permanent short circuits. Consequently, soft shorts may go undetected.[32–34,36]

EIS has been proposed as one diagnostic tool for identifying soft shorts.[34] The onset of a soft short is often marked by a gradual decrease in the bulk resistance of the cell during cycling, indicating the increasing presence of sodium dendrites within the electrolyte. These filaments allow some electrons to remain within the battery while others may flow to an external circuit, with ion flow between the electrodes continuing as well. Over time, the growth of these filaments can lead to a complete short circuit and cell failure. Therefore, monitoring impedance changes during cycling is important to gain insights into the onset and progression of soft shorts. In symmetric cells, a complete short-circuit (hard short-circuit) typically results in pure resistive behavior reflected in an EIS Nyquist spectrum as a linear response without an imaginary loop.[32] The case of soft short-circuits is more complex. Equivalent circuit model proposed by Menkin *et al.* to describe a soft short observation includes a charge-transfer resistor (R_{ct}), representing the electrode–electrolyte interface, in parallel with a lower-resistance element, the short-circuit resistor (R_{ss}), as illustrated in Fig. 11a.[32] The R_{ss} element represents the ability of electrons to flow through the formed short-circuit path between two Na electrodes. When the resistance of R_{ss} is sufficiently small, the system behaves like a pure resistor (equivalent to R_{sc}, Fig. 11a). However, if R_{ss} and R_{ct} are comparable, the cell may exhibit performance characteristics similar to those of a well-functioning battery, with a characteristic semicircle. In impedance spectra, the parallel R_{ss} results in a significant reduction in R_{ct}, and while the overpotential in the

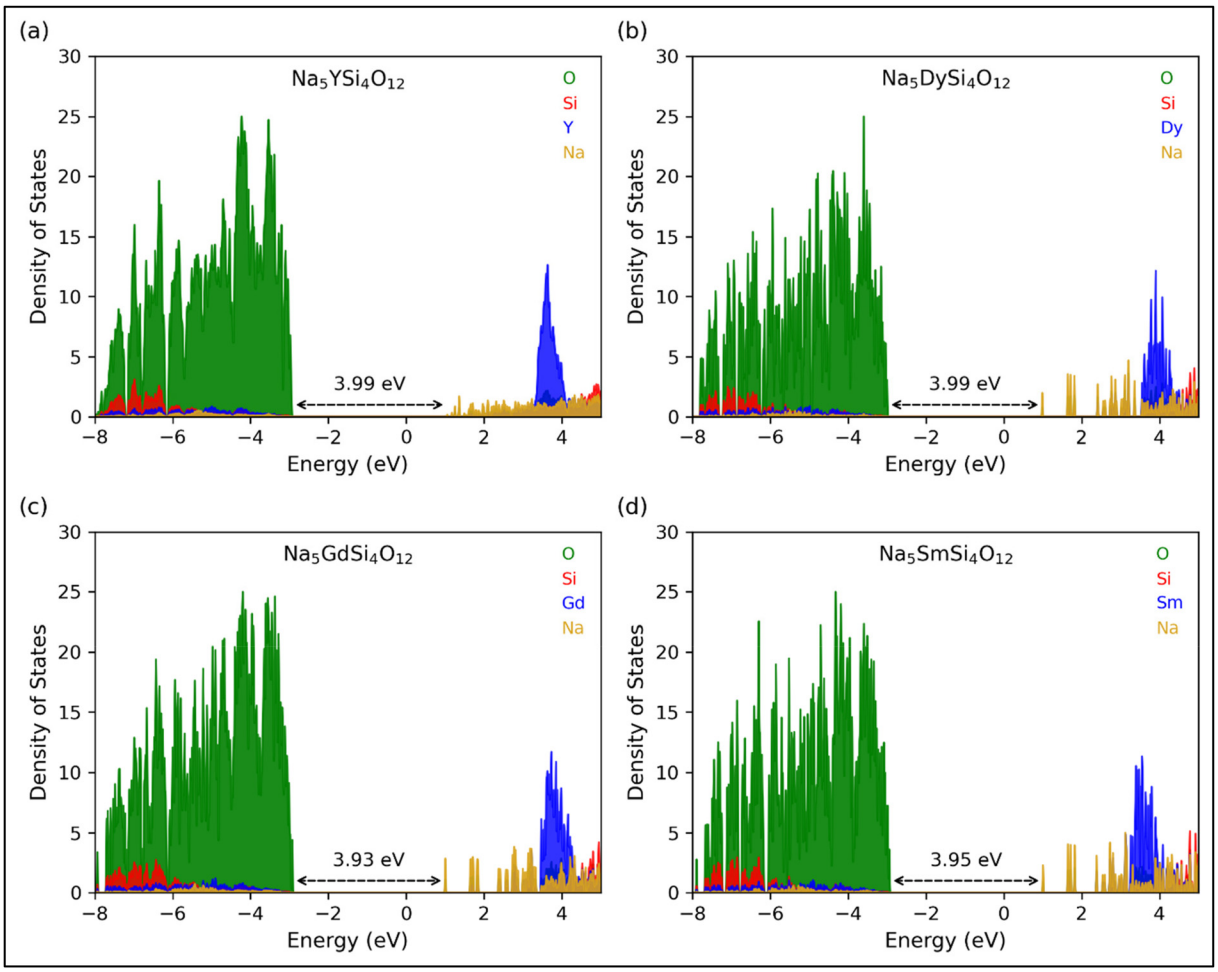

Fig. 12 DOS plot of (a) $Na_5YSi_4O_{12}$, (b) $Na_5DySi_4O_{12}$, (c) $Na_5GdSi_4O_{12}$ and (d) $Na_5SmSi_4O_{12}$. The valence band is dominated by O 2p states, while the conduction band primarily consists of rare-earth-derived states M 5d.

© 2026 The Author(s). Published by the Royal Society of Chemistry

Open Access Article. Published on 13 May 2026. Downloaded on 6/25/2026 9:59:45 AM. This article is licensed under a Creative Commons Attribution-NonCommercial 3.0 Unported Licence.

voltage–time profile decreases, it does not drop as drastically as in a complete short circuit. The voltage profile can also lack the rectangular shape typically associated with a full short-circuit, making the diagnosis of soft shorts more challenging.[32,34]

Based on observations of voltage profiles and EIS spectra, both Na/NYS/Na and Na/NDS/Na cells exhibit signs of soft shorting. Although the impedance did not reach 0 Ω, both cells show a linear response at negative imaginary impedance values in their post-cycling EIS spectra (Fig. 11b and c). In the Na/NYS/Na cell, a very subtle semicircle is observed at positive impedance values, suggesting that some charge transfer may still be present. Furthermore, the voltage profiles of both Na/NYS/Na and Na/NDS/Na cells show a drop in voltage (in the case of NDS, the cell briefly approached 0 V), yet after the drop, the systems continue to operate with declined performance, reflecting the increasing impact of the soft shorts. If the growth of sodium metal occurs slowly and there is a considerable ionic current even after an electronic pathway forms, the cell potential might decrease but not drop to zero as it would in the case of a 'hard' short. Once an electronic pathway forms, highly stable cycling may be observed. It is also important to note that soft shorts are dynamic.[32,34] Over-extended cycling, these pathways may gradually disappear, as the localised rise in current also increases temperature, causing the dendrite to dissolve back into the electrolyte. As a result, the cell restores its normal function and resumes cycling as expected.[37] A cell affected by a soft short can, after a period of rest, appear to behave normally again.[34] The EIS spectra for the studied symmetric cells were recorded immediately after the stripping/plating cycles, but the duration of this "recovery" period is unknown, which could explain why short circuits were not detected during the multimeter test. Therefore, further investigations are needed to fully understand the short-circuit behaviour of NYS and NSS solid electrolytes. In contrast, the EIS profile of Na/NSS/Na symmetric cell remains consistent, although with decreased resistance, suggesting that some sodium dendrites grow within the electrolyte. The voltage profile of the Na/NSS/Na cell at higher current rates is also stable and does not exhibit features typical of soft or complete short circuits (Fig. 11e). This was also the case for the Na/NGS/Na symmetric cell (Fig. 11d), suggesting that NSS and NGS are more resistant to sodium dendrite growth compared to NYS and NDS.

Electronic structure

First-principles calculations were conducted within the framework of density functional theory (DFT) to investigate the electronic structure of $Na_5MSi_4O_{12}$. Ordered structural models derived from the experimentally refined Na disorder were employed to ensure physically meaningful electronic structure descriptions. Fig. 12 shows the density of states (DOS) for $Na_5MSi_4O_{12}$ (M = Y, Dy, Gd, and Sm). For all compositions, a wide band gap of approximately 3.93–3.99 eV is observed, confirming the insulating nature of these materials. The valence band is dominated by O 2p states, with minor hybridisation with Si states, while the conduction band is primarily composed of rare-earth states, with some Si contribution. Importantly, Na-derived states are largely absent near both the valence band maximum and conduction band minimum, indicating that Na^+ ions do not contribute much to the electronic band gap but instead function as mobile ionic charge carriers.

Conclusions

We investigated the synthesis, phase stability, structure, ionic and electronic conductivities, chemical and electrochemical stability, interfacial resistance, and Na metal deposition of four highly conducting solid electrolytes in the NMS series: NYS, NDS, NGS, and NSS. The compounds are highly stable once they are synthesised. Rietveld analysis of synchrotron XRD data indicates that M-rich compositions of the N5 structure are favoured for smaller cations such as Y and Dy, whereas larger cations, such as Gd and especially Sm, lead to significant amounts of impurity phases. Further Na^+ ions will tend to occupy the M site as the size of the metal ion increases. The compounds are highly chemically stable in water and other aqueous media, demonstrating their compatibility with water-processable electrodes. They displayed high ionic conductivity with negligible electronic conductivity. They showed high stability with Na metal and reversible deposition, indicating their potential as solid electrolytes for solid-state sodium batteries. NGS and NSS can withstand higher current rates and exhibit smoother Na deposition. A wide band gap of approximately 3.93–3.99 eV is observed, confirming their compatibility with a wide range of electrode materials.

Experimental

Sodium carbonate (Na_2CO_3, 99.5%, Alfa Aesar), gadolinium oxide (Gd_2O_3, 99.9%, Thermo Scientific Chemicals), yttrium oxide (Y_2O_3, 99.9%, Thermo Scientific Chemicals), dysprosium oxide (Dy_2O_3, 99.9%, Thermo Scientific Chemicals), samarium oxide (Sm_2O_3, 99.9%, Thermo Scientific Chemicals) and silicon dioxide (SiO_2, 99.5%, Thermo Scientific Chemicals) were purchased from Thermo Fisher Scientific, UK.

The starting materials Na_2CO_3, Gd_2O_3, Y_2O_3, Dy_2O_3, Sm_2O_3 and SiO_2 were dried appropriately before use. Ball milling was performed using Fritsch Pulverisette 6 with ZrO_2 vials (80 mL). The ball-to-powder weight ratio was 10 : 1. Simultaneous Thermal Analysis (STA) measurements were performed on small amounts of both precursor and sintered NMS powder samples. The samples were placed in Al_2O_3 crucibles and analyzed using a Netzsch STA 449 F1 Jupiter instrument. Heating and cooling experiments were carried out under argon (Ar) atmosphere with a heating rate of 5 K min^{-1} over a temperature range from 35 to 1300 °C. The microstructure of the sintered solid electrolyte pellets was analysed using the scanning electron microscope Zeiss Evo LS25 SEM. Density measurements of the sintered pellets were performed according to

Open Access Article. Published on 13 May 2026. Downloaded on 6/25/2026 9:59:45 AM.
This article is licensed under a Creative Commons Attribution-NonCommercial 3.0 Unported Licence.

Archimedes' principle by suspending the samples in air and distilled water using a Kern EMB-V balance equipped with a density determination kit and measuring the resulting displacement. The experimental density was determined as the average of three independent measurements for each sample.

The phase purity of NGS, NYS, NDS, and NSS was determined by analyzing powder XRD patterns recorded on a Bruker D8 Discover diffractometer with Cu Kα radiation (40 kV; 40 mA). Scans were recorded between 10–60°. High-temperature X-ray diffraction (HTXRD) was performed on a Bruker D8 Discover diffractometer equipped with a Domed Hot Stage (DHS 1100, Anton Paar) fitted with a graphite dome. The diffractometer was operated with CuKα radiation (λ = 0.154 nm) using a Ni filter, an applied voltage of 40 kV, and a current of 40 mA. Diffraction patterns were collected over a 2θ range of 10–60° using a step size of 0.015° and a time of 1.0 s per step. Measurements were performed *in situ* over the temperature range 700–1100 °C. The specimen was first heated to 700 °C at 5 °C min^{-1}, held at this temperature for 3 h, and XRD patterns were recorded under the conditions described above. Diffraction patterns were collected at 800, 900, 1000, 1050, and 1100 °C. For each step, the sample was heated to the target temperature at 3 °C min^{-1}, followed by a 30 minute isothermal hold before the scan was recorded. After completion of the high-temperature measurements, the sample was cooled to room temperature under natural cooling conditions, and a final diffraction pattern was recorded at 30 °C. The high-resolution synchrotron X-ray diffraction was performed at beamline ID31 at the European Synchrotron Radiation Facility (ESRF) using an incident X-ray energy of 75.051 keV (λ = 0.16520 Å). Sample powders are loaded into cylindrical slots (approx. 1 mm thickness) held between Kapton windows in a high-throughput sample holder. Measurements are conducted in transmission geometry using a Pilatus CdTe 2M detector positioned with the incident beam in the corner of the detector. Background measurements for the empty windows are measured and subtracted. NIST SRM 660b (LaB_6) is used for geometry calibration performed with pyFAI software, followed by image integration, including flat-field, geometry, solid-angle, and polarization corrections. Automated background subtraction is taken, and parallax correction is performed based on Rietveld refinement of LaB_6 660b.

Rietveld analysis was performed with TOPAS 6 (Bruker) using a modified fundamental parameters approach, with instrumental broadening determined from reference scans. Sample-related broadening was modeled by using Voigt functions with $\cos^{-1}(\theta)$ and $\tan(\theta)$ angular dependence of broadening to adjust for crystallite size and macrostrain effects on the reflection profile, respectively. Isotropic displacement parameters were constrained to be identical for all chemically identical ions (*e.g.* B(Na1) = B(Na2) = B(Na3) ...; B(Si1) = B(Si2)); *etc.*; only for the Na(6) site, a different and higher B value was allowed to be refined, related to the low degree of localization of the anions of this site. Overall compositions were constrained to follow a composition of $Na_{(2-3x)*n}M_{x*n}(SiO_3)_n$. Although indexing attempts were performed, impurity phases visible in the synchrotron data for all samples could not be identified with any known phases reported in the ICSD or ICDD databases. To approximate the amounts of impurity phases in the different materials, reflections from unidentified phases were fitted with Voigt functions to estimate their integral intensities. The amount of impurity phases was then determined by relating the integral intensity of reflections belonging to phases other than the N5 phase (unknown and N9) to the sum of all reflection intensities.

For Electrochemical Impedance Spectroscopy (EIS) measurements, gold (Au) was sputtered as a blocking electrode on either side of the SE discs using an Agar sputter coater. EIS was performed using a Gamry 1010E potentiostat, with an AC frequency range of 10 mHz to 2 MHz and an alternating voltage amplitude of 10 mV. Ionic conductivities were obtained by fitting the resulting impedance spectra. The temperature-dependent impedance between RT and 120 °C was recorded to determine the activation energy (E_a). For chronopotentiometry measurements, Na metal discs were freshly prepared for each assembled cell in an Ar-filled MBraun glovebox (O_2 < 0.5 ppm, H_2O < 0.5 ppm). A clean piece of Na was cut from a rod (Na sticks, covered in a film of protective hydrocarbon oil, 99% Alfa Aesar), then pressed flat and cut into circular electrodes. The surface of the Na disc was mechanically cleaned using a scalpel blade to expose the fresh metal. The Na metal electrodes were then placed on both sides of the solid electrolyte pellet, and the other side of each Na disc was covered with Al foil. The Na/SE/Na stack was pressed by hand and assembled in the modified Swagelok cell inside the glovebox. Assembled cells were placed in an incubator at 25 °C to maintain the temperature. Chronopotentiometry studies were performed using a Gamry 1010E potentiostat. Galvanostatic cycling was performed to test the stability of Na^+ plating/stripping, increasing the current density from 0.1 to 0.5 mA cm^{-2} every 8 h. The current direction was reversed every 0.5 h. The electrochemical window of the solid electrolyte was studied using linear sweep voltammetry. Asymmetric cells with an NMS pellet sandwiched between a Na metal disc (acting as the reversible electrode) and a stainless steel (SS) current collector (acting as the blocking electrode) were assembled in an Ar-filled MBraun glovebox (O_2 < 0.5 ppm, H_2O < 0.5 ppm). The voltametric range for the LSV measurement was between the open-circuit voltage (~1.9 V) and 8 V (*vs.* Na^+/Na), and the scan rate was 0.1 mV s^{-1}. Electronic conductivity of the NMS solid electrolytes was determined by DC polarisation using blocking gold electrodes in an Au/NMS/Au configuration assembled in a modified Swagelok-type cell inside an Ar-filled glovebox. DC polarisation was performed at room temperature using a Gamry Reference 1010E potentiostat by applying a constant potential of 0.2 V for 8 h. Data were analysed using Gamry Echem Analyst.

Phase stability and structural ordering

The refined crystal structures of $Na_5YSi_4O_{12}$, $Na_5GdSi_4O_{12}$, $Na_5DySi_4O_{12}$, and $Na_5SmSi_4O_{12}$ exhibit partial occupancies at the Na sites. To construct ordered structural models, Na configurations consistent with the experimental stoichiometry

© 2026 The Author(s). Published by the Royal Society of Chemistry

Open Access Article. Published on 13 May 2026. Downloaded on 6/25/2026 9:59:45 AM. This article is licensed under a Creative Commons Attribution-NonCommercial 3.0 Unported Licence.

were generated using an electrostatic energy minimisation scheme implemented in the Python Materials Genomics (pymatgen) framework.[38] Approximately 40 lowest-energy configurations for each compound were selected and subsequently fully relaxed using density functional theory (DFT). The lowest-energy DFT-relaxed structures were identified as the ground-state configurations and were used for all subsequent analyses.

Density functional theory computations

All density functional theory (DFT) calculations were performed using the Quantum ESPRESSO (QE) package[39,40] within the projector augmented wave (PAW) approach. The generalised gradient approximation (GGA) with the Perdew–Burke–Ernzerhof (PBE) exchange–correlation functional was employed for total-energy and density-of-states (DOS) calculations. Brillouin zone sampling was carried out using a Monkhorst–Pack *k*-point mesh of 2 × 2 × 4. The plane-wave kinetic energy cutoff and charge density cutoff were set to 60 Ry and 480 Ry, respectively. Calculations were performed in a non-spin-polarised framework. Pseudopotentials were obtained from the Quantum ESPRESSO pseudopotential database.[41] For the rare-earth elements, PAW pseudopotentials with the 4f electrons treated as frozen core states were used, as the electronic states near the Fermi level are dominated by M 5d (M = Dy, Gd, Sm) and O 2p orbitals.

Author contributions

MAR planned the study; AM performed the experiments; TD performed the high-temperature XRD; OC did the refinement and structural analysis; UU performed the theoretical calculations; MAR and AM wrote the manuscript with the help of UU and OC. All authors reviewed the manuscript.

Conflicts of interest

The authors declare no competing interests.

Data availability

The data supporting this article are included in the supplementary information (SI). See DOI: https://doi.org/10.1039/d6eb00059b.

Acknowledgements

We gratefully acknowledge funding from the Engineering and Physical Sciences Research Council (EPSRC) under grant EP/V014994/1. The authors also acknowledge access to characterisation equipment at the Swansea University Advanced Imaging of Materials (AIM) facility, which was funded in part by the EPSRC (EP/M028267/1) and the European Regional Development Fund through the Welsh Government (80708). The authors further thank Professor Nicholas Lavery and Dr Shahin Mehraban for conducting the STA measurements at the Swansea University Materials Advanced Characterisation Centre (MACH1), which was funded through the ERDF A4B programme.

References

1 T. Famprikis, P. Canepa, J. A. Dawson, M. S. Islam and C. Masquelier, Fundamentals of inorganic solid-state electrolytes for batteries, *Nat. Mater.*, 2019, **18**(12), 1278–1291, DOI: 10.1038/s41563-019-0431-3.

2 Y. Dong, P. Wen, H. Shi, Y. Yu and Z.-S. Wu, Solid-State Electrolytes for Sodium Metal Batteries: Recent Status and Future Opportunities, *Adv. Funct. Mater.*, 2024, **34**(5), 2213584, DOI: 10.1002/adfm.202213584.

3 H.-L. Yang, B.-W. Zhang, K. Konstantinov, Y.-X. Wang, H.-K. Liu and S.-X. Dou, Progress and Challenges for All-Solid-State Sodium Batteries, *Adv. Energy Sustainability Res.*, 2021, **2**(2), 2000057, DOI: 10.1002/aesr.202000057.

4 T. Fuchs, S. P. Culver, P. Till and W. G. Zeier, Defect-Mediated Conductivity Enhancements in Na3−xPn1−xWxS4 (Pn = P, Sb) Using Aliovalent Substitutions, *ACS Energy Lett.*, 2020, **5**(1), 146–151, DOI: 10.1021/acsenergylett.9b02537.

5 Z. Li, P. Liu, K. Zhu, Z. Zhang, Y. Si, Y. Wang and L. Jiao, Solid-State Electrolytes for Sodium Metal Batteries, *Energy Fuels*, 2021, **35**(11), 9063–9079, DOI: 10.1021/acs.energyfuels.1c00347.

6 Q. Ma and F. Tietz, Solid-State Electrolyte Materials for Sodium Batteries: Towards Practical Applications, *ChemElectroChem*, 2020, **7**(13), 2693–2713, DOI: 10.1002/celc.202000164.

7 N. Baffier, J. C. Badot and P. Colomban, Conductivity of ion rich β and β″ alumina: Sodium and potassium compounds, *Mater. Res. Bull.*, 1981, **16**(3), 259–265, DOI: 10.1016/0025-5408(81)90040-4.

8 M. P. Fertig, K. Skadell, M. Schulz, C. Dirksen, P. Adelhelm and M. Stelter, From High- to Low-Temperature: The Revival of Sodium-Beta Alumina for Sodium Solid-State Batteries, *Batteries Supercaps*, 2022, **5**(1), e202100131, DOI: 10.1002/batt.202100131.

9 X. Lu, G. Xia, J. P. Lemmon and Z. Yang, Advanced materials for sodium-beta alumina batteries: Status, challenges and perspectives, *J. Power Sources*, 2010, **195**(9), 2431–2442, DOI: 10.1016/j.jpowsour.2009.11.120.

10 F. G. Will, Effect of Water on Beta Alumina Conductivity, *J. Electrochem. Soc.*, 1976, **123**(6), 834, DOI: 10.1149/1.2132943.

11 J. B. Goodenough, H. Y. P. Hong and J. A. Kafalas, Fast Na+-ion transport in skeleton structures, *Mater. Res. Bull.*, 1976, **11**(2), 203–220, DOI: 10.1016/0025-5408(76)90077-5.

12 Y. Li, M. Li, Z. Sun, Q. Ni, H. Jin and Y. Zhao, Recent advance on NASICON electrolyte in solid-state sodium metal batteries, *Energy Storage Mater.*, 2023, **56**, 582–599, DOI: 10.1016/j.ensm.2023.01.047.

13 A. U. I. Gebi, O. Dolokto, L. Mereacre, U. Geckle, H. Radinger, M. Knapp and H. Ehrenberg, Characterization

Open Access Article. Published on 13 May 2026. Downloaded on 6/25/2026 9:59:45 AM. This article is licensed under a Creative Commons Attribution-NonCommercial 3.0 Unported Licence.

and Comparative Study of Energy Efficient Mechanochemically Induced NASICON Sodium Solid Electrolyte Synthesis, *ChemSusChem*, 2024, **17**(2), e202300809, DOI: 10.1002/cssc.202300809.

14 R. D. Shannon, B. E. Taylor, T. E. Gier, H. Y. Chen and T. Berzins, Ionic conductivity in sodium yttrium silicon oxide (Na5YSi4O12)-type silicates, *Inorg. Chem.*, 1978, **17**(4), 958–964, DOI: 10.1021/ic50182a033.

15 F. C. Lee, J. Marr and F. P. Glasser, Compounds in the Na2O·Y2O3·SiO_2 system, *Ceram. Int.*, 1981, **7**(2), 43–47, DOI: 10.1016/0272-8842(81)90012-2.

16 R. D. Shannon, T. E. Gier, C. M. Foris, J. A. Nelen and D. E. Appelman, Crystal data for some sodium rare earth silicates, *Phys. Chem. Miner.*, 1980, **5**(3), 245–253, DOI: 10.1007/BF00348573.

17 K. Yamashita, T. Nojiri, T. Umegaki and T. Kanazawa, New fast sodium-ion conducting glass-ceramics of silicophosphates: Crystallization, microstructure and conduction properties, *Solid State Ion.*, 1989, **35**(3), 299–306, DOI: 10.1016/0167-2738(89)90312-3.

18 K. Yamashita, S. Ohkura, T. Umegaki and T. Kanazawa, Synthesis, Polymorphs and Sodium Ionic Conductivity of Sodium Yttrium Silicophosphates with the Composition, *J. Ceram. Soc. Jpn.*, 1988, **96**(1118), 967–972, DOI: 10.2109/jcersj.96.967.

19 K. Yamashita, M. Tanaka and T. Umegaki, Thermodynamic and kinetic study on the phase transformation of the glass-ceramic Na+ superionic conductors Na3+3x−yRe1−xPySi3−yO9, *Solid State Ion.*, 1992, **58**(3), 231–236, DOI: 10.1016/0167-2738(92)90123-7.

20 H.-B. Sun, J.-Z. Guo, Y. Zhang, T. Wei, Y.-X. Zhou, L.-L. Zhang, X.-L. Wu, Y. Huang and W. Luo, High-Voltage All-Solid-State Na-Ion-Based Full Cells Enabled by All NASICON-Structured Materials, *ACS Appl. Mater. Interfaces*, 2019, **11**(27), 24192–24197, DOI: 10.1021/acsami.9b07647.

21 G. Sun, X. Yang, N. Chen, S. Yao, X. Wang, X. Jin, G. Chen, Y. Xie and F. Du, Na5YSi4O12: A sodium superionic conductor for ultrastable quasi-solid-state sodium-ion batteries, *Energy Storage Mater.*, 2021, **41**, 196–202, DOI: 10.1016/j.ensm.2021.06.003.

22 A. Yang, R. Ye, H. Song, Q. Lu, X. Wang, E. Dashjav, K. Yao, D. Grüner, Q. Ma, F. Tietz, *et al.*, Pressureless all-solid-state Na/S batteries with self-supporting Na5YSi4O12 scaffolds, *Carbon Energy*, 2023, **5**(12), e371, DOI: 10.1002/cey2.371.

23 N. Xu, C. Yuan, G. Sun, N. Chen, S. Yao and F. Du, Na5YSi4O12 fast ion conductor protection layer enabled dendrite-free Zn metal anode, *Carbon Neutrality*, 2023, **2**(1), 33, DOI: 10.1007/s43979-023-00073-5.

24 A. Yang, R. Ye, X. Li, Q. Lu, H. Song, D. Grüner, Q. Ma, F. Tietz, D. Fattakhova-Rohlfing and O. Guillon, Fabrication of thin sheets of the sodium superionic conductor Na5YSi4O12 with tape casting, *Chem. Eng. J.*, 2022, **435**, 134774, DOI: 10.1016/j.cej.2022.134774.

25 A. Michalak, S. M. Behara and M. Anji Reddy, Reinvestigation of Na5GdSi4O12: A Potentially Better Solid Electrolyte than Sodium β Alumina for Solid-State Sodium Batteries, *ACS Appl. Mater. Interfaces*, 2024, **16**(6), 7112–7118, DOI: 10.1021/acsami.3c16153.

26 G. Sun, C. Lou, B. Yi, W. Jia, Z. Wei, S. Yao, Z. Lu, G. Chen, Z. Shen, M. Tang and F. Du, Electrochemically induced crystalline-to-amorphization transformation in sodium samarium silicate solid electrolyte for long-lasting sodium metal batteries, *Nat. Commun.*, 2023, **14**, 6501, DOI: 10.1038/s41467-023-42308-0.

27 B. Yi, Z. Wei, W. Jia, G. Sun, W. Si, S. Yao, G. Chen and F. Du, Nonstoichiometry Induced Amorphous Grain Boundary of Na5SmSi4O12 Solid-State Electrolyte for Long-Life Dendrite-Free Sodium Metal Battery, *Nano Lett.*, 2024, **24**(29), 8911–8919, DOI: 10.1021/acs.nanolett.4c01743.

28 D. M. Többens, V. Kahlenberg, R. Kaindl, B. Sartory and J. Konzett, Na8.25Y1.25Si6O18 and its family of zwölfer ring silicates, *Z. Kristallogr. – Cryst. Mater.*, 2008, **223**(6), 389–398, DOI: 10.1524/zkri.2008.0039.

29 B. A. Maksimov, V. R. Kalinin, B. V. Merinov, V. V. Ilyukhin and N. V. Belov, Crystal structure of rare earth Na, Y-metasilicate [Na3YSi3O9]x4=Na12Y4[Si12O36]infinity, *Dokl. Akad. Nauk SSSR*, 1980, **252**(4), 875–879.

30 R. D. Shannon, Revised effective ionic radii and systematic studies of interatomic distances in halides and chalcogenides, *Acta Crystallogr., Sect. A*, 1976, **32**(5), 751–767, DOI: 10.1107/S0567739476001551.

31 H. U. Beyeler and T. Hibma, The sodium conductivity paths in the superionic conductors Na5RESi4O12, *Solid State Commun.*, 1978, **27**(6), 641–643, DOI: 10.1016/0038-1098(78)90461-1.

32 S. Menkin, J. B. Fritzke, R. Larner, C. de Leeuw, Y. Choi, A. B. Gunnarsdóttir and C. P. Grey, Insights into soft short circuit-based degradation of lithium metal batteries, *Faraday Discuss.*, 2024, **248**, 277–297, DOI: 10.1039/D3FD00101F.

33 M. J. Counihan, K. S. Chavan, P. Barai, D. J. Powers, Y. Zhang, V. Srinivasan and S. Tepavcevic, The phantom menace of dynamic soft-shorts in solid-state battery research, *Joule*, 2024, **8**(1), 64–90, DOI: 10.1016/j.joule.2023.11.007.

34 Q. Li, A. Chen, D. Wang, Z. Pei and C. Zhi, "Soft Shorts" Hidden in Zinc Metal Anode Research, *Joule*, 2022, **6**(2), 273–279, DOI: 10.1016/j.joule.2021.12.009.

35 L. Ma, M. A. Schroeder, O. Borodin, T. P. Pollard, M. S. Ding, C. Wang and K. Xu, Realizing high zinc reversibility in rechargeable batteries, *Nat. Energy*, 2020, **5**(10), 743–749, DOI: 10.1038/s41560-020-0674-x.

36 C. Wang, T. Deng, X. Fan, M. Zheng, R. Yu, Q. Lu, H. Duan, H. Huang, C. Wang and X. Sun, Identifying soft breakdown in all-solid-state lithium battery, *Joule*, 2022, **6**(8), 1770–1781, DOI: 10.1016/j.joule.2022.05.020.

37 E. Winter, T. J. Schmidt and S. Trabesinger, Identifying Pitfalls in Lithium Metal Battery Characterization, *Batteries Supercaps*, 2022, **5**(1), e202100145, DOI: 10.1002/batt.202100145.

38 S. P. Ong, W. D. Richards, A. Jain, G. Hautier, M. Kocher, S. Cholia, D. Gunter, V. L. Chevrier, K. A. Persson and G. Ceder, Python Materials Genomics (pymatgen): A

© 2026 The Author(s). Published by the Royal Society of Chemistry

Open Access Article. Published on 13 May 2026. Downloaded on 6/25/2026 9:59:45 AM.
This article is licensed under a Creative Commons Attribution-NonCommercial 3.0 Unported Licence.

Robust, Open-Source Python Library for Materials Analysis, *Comput. Mater. Sci.*, 2013, **68**, 314–319, DOI: 10.1016/j.commatsci.2012.10.028.

39 P. Giannozzi, S. Baroni, N. Bonini, M. Calandra, R. Car, C. Cavazzoni, D. Ceresoli, G. L. Chiarotti, M. Cococcioni, I. Dabo, A. Dal Corso, S. Fabris, G. Fratesi, S. de Gironcoli, R. Gebauer, U. Gerstmann, C. Gougoussis, A. Kokalj, M. Lazzeri, L. Martin-Samos, N. Marzari, F. Mauri, R. Mazzarello, S. Paolini, A. Pasquarello, L. Paulatto, C. Sbraccia, S. Scandolo, G. Sclauzero, A. P. Seitsonen, A. Smogunov, P. Umari and R. M. Wentzcovitch, QUANTUM ESPRESSO: A Modular and Open-Source Software Project for Quantum Simulations of Materials, *J. Phys.: Condens. Matter*, 2009, **21**(39), 395502, DOI: 10.1088/0953-8984/21/39/395502.

40 P. Giannozzi, O. Andreussi, T. Brumme, O. Bunau, M. Buongiorno Nardelli, M. Calandra, R. Car, C. Cavazzoni, D. Ceresoli, M. Cococcioni, N. Colonna, I. Carnimeo, A. Dal Corso, S. de Gironcoli, P. Delugas, R. A. DiStasio Jr, A. Ferretti, A. Floris, G. Fratesi, G. Fugallo, R. Gebauer, U. Gerstmann, F. Giustino, T. Gorni, J. Jia, M. Kawamura, H.-Y. Ko, A. Kokalj, E. Küçükbenli, M. Lazzeri, M. Marsili, N. Marzari, F. Mauri, N. L. Nguyen, H.-V. Nguyen, A. Otero-de-la-Roza, L. Paulatto, S. Poncé, D. Rocca, R. Sabatini, B. Santra, M. Schlipf, A. P. Seitsonen, A. Smogunov, I. Timrov, T. Thonhauser, P. Umari, N. Vast, X. Wu and S. Baroni, Advanced Capabilities for Materials Modelling with Quantum ESPRESSO, *J. Phys.: Condens. Matter*, 2017, **29**(46), 465901, DOI: 10.1088/1361-648X/aa8f79.

41 We used the pseudopotentials Na.pbe-spn-kjpaw_psl.1.0.0.UPF, Si.pbe-n-kjpaw_psl.1.0.0.UPF, O.pbe-n-kjpaw_psl.1.0.0.UPF, Y.pbe-spn-kjpaw_psl.1.0.0.UPF, Sm.pbe-spdn-kjpaw_psl.1.0.0.UPF, Gd.pbe-spdn-kjpaw_psl.1.0.0.UPF and Dy.pbe-spdn-kjpaw_psl.1.0.0.UPF from the Quantum ESPRESSO pseudopotential data base: https://www.quantum-espresso.org/pseudopotentials.